

High Cooperativity Using a Confocal-Cavity–QED Microscope

Ronen M. Kroeze,^{1,2} Brendan P. Marsh,^{2,3} Kuan-Yu Lin,^{1,2} Jonathan Keeling^{1b,4} and Benjamin L. Lev^{1b,2,3,*}

¹*Department of Physics, Stanford University, Stanford, California 94305, USA*

²*E. L. Ginzton Laboratory, Stanford University, Stanford, California 94305, USA*

³*Department of Applied Physics, Stanford University, Stanford, California 94305, USA*

⁴*SUPA, School of Physics and Astronomy, University of St. Andrews, St. Andrews KY16 9SS, United Kingdom*

 (Received 15 December 2022; accepted 11 April 2023; published 11 May 2023; corrected 5 July 2023)

Cavity quantum electrodynamics (QED) with cooperativity far greater than unity enables high-fidelity quantum sensing and information processing. The high-cooperativity regime is often reached through the use of short single-mode resonators. More complicated multimode resonators, such as the near-confocal optical Fabry–Pérot cavity, can provide intracavity atomic imaging in addition to high cooperativity. This capability has recently proved important for exploring quantum many-body physics in the driven-dissipative setting. In this work, we show that a confocal-cavity–QED microscope can realize cooperativity in excess of 110. This cooperativity is on par with the very best single-mode cavities (which are far shorter) and 21 times greater than single-mode resonators of similar length and mirror radii. The 1.7- μm imaging resolution is naturally identical to the photon-mediated interaction range. We measure these quantities by determining the threshold of cavity superradiance when small optically tweezed Bose-Einstein condensates are pumped at various intracavity locations. Transmission measurements of an *ex situ* cavity corroborate these results. We provide a theoretical description that shows how cooperativity enhancement arises from the dispersive coupling to the atoms of many near-degenerate modes.

DOI: [10.1103/PRXQuantum.4.020326](https://doi.org/10.1103/PRXQuantum.4.020326)

I. INTRODUCTION

Strong light-matter interactions allow for the coherent exchange of quantum information between photonic and atomic degrees of freedom. Because exchange can occur before decoherence from dissipation, strong coupling is a key ingredient in many quantum information and sensing platforms [1–5]. Moreover, it also allows photonic excitations to be coherently exchanged among atoms in such a way as to mediate particle or spin interactions [6–15]. These can induce nonequilibrium quantum many-body phases [16].

Optical-cavity quantum electrodynamics (QED) provides the means to generate strong coupling through the interaction of the electric dipole of an atom with the electromagnetic field confined as a cavity mode [18]. The larger the field, the stronger is the coupling. Single-mode resonators are typically employed to enhance the field

at the atom. However, multimode degenerate cavities are of increasing interest [19,20]. They accommodate many modes at (nearly) the same resonant frequency [17] and thereby enable light-matter coupling involving the participation of spatially distinct modes. A wealth of exotic phenomena can result, including (interacting) photonic Laughlin states [21], optical mode conversion [22], and compliant optical lattices [20] arising from emergent crystallinity [6,20,23]. These arise from interactions of tunable range and connectivity [9,10] as well as from broken continuous symmetries induced by the cavity coupling [11]. Tunable connectivity can also be realized using multifrequency-driven single-mode cavities [13,24,25], and a $U(1)$ symmetry may be broken in ring [6,23,26,27] or crossed single-mode cavities [28,29]. Other applications such as the simulation of synthetic pairing [30] and dynamical gauge fields [31], spin glasses [7,32–34], and neuro-morphic optimizers (enabling, e.g., associative memory) [35–38] may arise from the unique nonlocal interactions provided by multimode cavity QED [9,10].

The relative strength of light-matter interactions in a single-mode cavity is captured by the cooperativity C [18,39]. This figure of merit compares the single-atom single-photon interaction strength g_0 to two dissipative rates through the ratio $C \equiv g_0^2/\kappa\gamma_{\perp}$ [40]. Field dissipation

*benlev@stanford.edu

Published by the American Physical Society under the terms of the [Creative Commons Attribution 4.0 International license](https://creativecommons.org/licenses/by/4.0/). Further distribution of this work must maintain attribution to the author(s) and the published article's title, journal citation, and DOI.

at the rate κ occurs due to emission through the cavity mirrors (and absorption therein). Atomic decoherence proceeds via free-space spontaneous emission at the rate γ_{\perp} . For a two-level atom, $\gamma_{\perp} = \Gamma/2$, where Γ is the population decay rate. The strong-coupling regime arises when $C > 1$ and high-fidelity quantum state preparation usually requires $C \gg 1$ [1]. In this regime, coherent mixing of atomic and photonic excitations is sufficiently strong to generate quantum entanglement [41], effects such as photon blockade [42], and coupling to Rydberg atoms [43,44].

The cooperativity of a Fabry-Pérot cavity is inversely proportional to the transverse-mode area at the atom [39]. A common strategy to raise C involves reducing the mode waist w_0 . This can be accomplished by shrinking the length of optical single-mode cavities to the hundred-micron regime or less. By contrast, multimode cavities can provide small effective mode waists while maintaining large cavity lengths for easy transverse access and small κ (if desirable). This leads to an enhanced light-matter interaction strength g . We define the multimode cooperativity as $C_{\text{mm}} = g^2/\kappa\gamma_{\perp}$. C_{mm} plays the same figure-of-merit role as C does for single-mode cavities.

Single-mode cavities support TEM_{lm} modes that are spaced in frequency much further than any other scale. Relevant scales include g_0 , κ , and the detuning $\Delta_C = \omega_P - \omega_C$ between the pump ω_P and cavity ω_C fields. By contrast, multimode cavities exhibit a large (near-)degeneracy of modes within a bandwidth $\omega_B \leq \Delta_C$. Concentric cavities are a particularly simple example. However, practicable cavities cannot reach the concentric limit at which the cavity length L equals twice the radius of curvature R of its mirrors without becoming unstable [17]. By contrast, the confocal cavity ($L = R$) is stable in practice. This resonator geometry provides a narrow mode waist, even for L values as large as 1 cm, as we demonstrate in this work.

We experimentally show how a confocal cavity can enable the creation of an electric field of narrow waist at the position of intracavity atoms coupled to a transverse pump field [see Fig. 1(a)]. This provides access to the high-cooperativity limit: The cavity enables ^{87}Rb atoms that are pumped on the D_2 atomic transition to couple to light with a multimode cooperativity of $C_{\text{mm}} = 112(2)$, because the mode waist can shrink to $w_{\text{eff}} = 1.7(2) \mu\text{m}$ [45]. As explained in detail below, this is possible because the cavity can support a localized photonic wave packet that matches the size and position of the atomic gas. That is, the confocal cavity can superimpose the electric fields of many (near-)degenerate modes into a concentrated area at the atomic position. For comparison, this waist is far smaller than the Gaussian TEM_{00} waist $w_0 = 35 \mu\text{m}$ of a single-mode cavity with the same R and nearly the same length. If such a cavity has the same finesse, then it will yield a C of only 5.2. A cooperativity of 110 is on par with the much shorter state-of-the-art single-mode cavities that have been employed for quantum gas

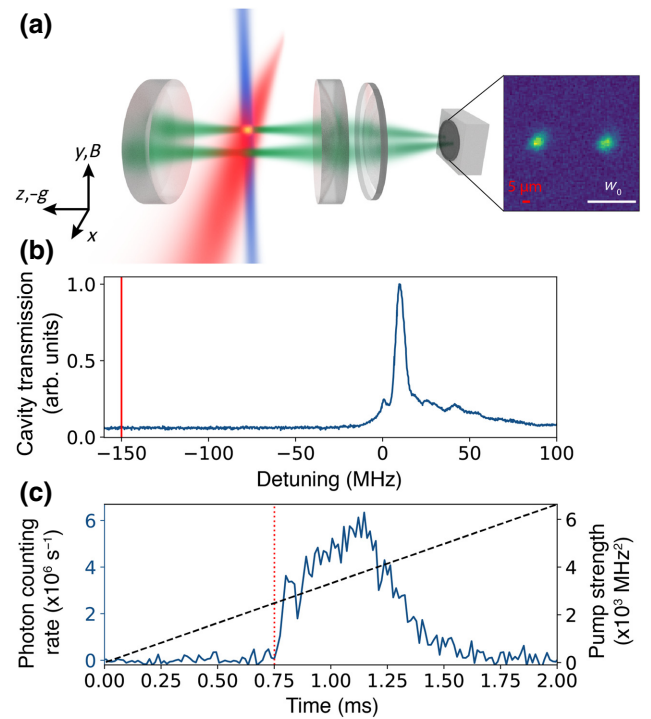


FIG. 1. (a) An illustration of the experiment. An ^{87}Rb Bose-Einstein condensate (BEC) (orange) is positioned using an optical-tweezer dipole trap (blue) inside a confocal cavity. It is pumped by a transverse running-wave laser (red), which induces a superradiant self-organization phase transition above a critical pump power. This scatters light into a synthetic mode—i.e., a near-degenerate mode superposition—of the cavity (green), which can be imaged onto a detector (gray box). The single synthetic mode cavity field appears as two green beams or spots because the crossed “nonlocal” portion connecting them is far less intense than the straight “local” portions shown in the figure [17]. The inset image shows an example of the synthetic mode emission; the two spots correspond to the image and mirror components of the local field and demonstrate the ability of the cavity to image the BEC. The waist of the fundamental mode of the cavity is $w_0 = 35 \mu\text{m}$. (b) The transmission spectrum of the employed confocal cavity taken by using a probe beam focused at the cavity center with a waist of $25 \mu\text{m}$ (at the cavity midplane). The red line indicates a typical transverse pump detuning from a reference point within the mode spread ω_B , here chosen to be the first local maximum in the transmission. (c) An example of the cavity emission (solid blue) detected by a single-photon counter versus time. The pump power is shown as a dashed black line. The threshold power is indicated by the red dotted line. Superradiant emission is observed once the threshold is reached and persists for $\lesssim 1$ ms, limited by the excitation of atomic motion by the running-wave pump.

cavity QED (cQED) [16,46]. In this work, the cooperativity is measured through its effect on the threshold of cavity superradiance induced by transversely pumping an intracavity Bose-Einstein condensate (BEC). We qualitatively explain this effect in Sec. II, before describing the

measurement scheme and experimental results on cooperativity enhancement in Secs. III and IV, respectively. A study of the optical resolution of an *ex situ* confocal cavity of the same configuration corroborates these results and is presented in Sec. V. The thresholds are connected to cooperativity enhancement by using the theoretical description presented in Appendix A. Appendices B and C present details of the data-fitting procedure and the *ex situ* cavity measurement, respectively. The estimate of the number of modes coupled to the atoms is presented in Appendix D.

II. COOPERATIVITY ENHANCEMENT THROUGH MODE SUPERPOSITION

We now describe the mechanism by which the cooperativity is enhanced in a confocal cavity. Multimode cavity QED, of which the confocal configuration is one instance, allows the atoms inside the cavity to dynamically shape the electric field modes to which it couples. Above a threshold pump power, the atoms maximize the field at their position by way of a superradiant phase transition [47]. This leads to an enhancement of light-matter coupling. To explain this effect—and the measurements we report later—we must first consider the Green's function of an idealized confocal cavity, one in which all mode families are perfectly degenerate [17]. We then consider the case involving practicable resonators.

A. Ideal multimode cavities

Cavity modes are often represented in a Hermite-Gaussian basis consisting of nonlocal mode functions. We denote them by their transverse field profile $\Xi_\mu(\mathbf{r})$, where the $\mu = \{l_\mu, m_\mu\}$ are transverse mode indices. However, an equally valid basis for degenerate cavities consists of local mode functions that tile the cavity midplane, located at $z = 0$ [48]. A cavity supporting an infinite number of degenerate modes will admit superpositions of the $\Xi_\mu(\mathbf{r})$ that form delta functions at each point in the midplane. Each element of this re-diagonalized mode basis may be referred to as a supermode. An atom couples to the supermode formed at its location (\mathbf{r}, z) .

The steady-state cavity field $\Phi(\mathbf{r}, z)$ that arises due to scattering of the pump into the cavity is, to lowest order,

$$\Phi(\mathbf{r}, z) = \Phi_0 \int d\mathbf{r}' dz' \mathcal{D}(\mathbf{r}, \mathbf{r}', z, z') \rho(\mathbf{r}', z'), \quad (1)$$

where the atomic distribution is $\rho(\mathbf{r}, z)$ and is normalized by $\int \rho(\mathbf{r}, z) d\mathbf{r} dz = 1$, $\mathcal{D}(\mathbf{r}, \mathbf{r}', z, z')$ is the cavity Green's function and Φ_0 is the scaled field strength given in Appendix A. As we show in Appendix A 3, the maximum multimode cooperativity C_{mm} is set by the strength of the cavity field at the location of a point source, that is,

$$\frac{C_{\text{mm}}}{C} = \max_{\mathbf{r}, z} \frac{\Phi(\mathbf{r}, z)}{\Phi_0} = \max_{\mathbf{r}, z} \mathcal{D}(\mathbf{r}, \mathbf{r}, z, z). \quad (2)$$

For a confocal cavity, this maximum is at the cavity center and $C_{\text{mm}}/C = \mathcal{D}(\mathbf{0}, \mathbf{0}, 0, 0)$. The general expression for this Green's function is

$$\mathcal{D}(\mathbf{r}, \mathbf{r}', z, z') = \sum_{\mu} W_{\mu} \Xi_{\mu}(\mathbf{r}) \Xi_{\mu}(\mathbf{r}') \times \cos[kz - \theta_{\mu}(z)] \cos[kz' - \theta_{\mu}(z')], \quad (3)$$

where the longitudinal mode phase is $\theta_{\mu}(z)$ and W_{μ} is the weight of each mode in the superposition [10, 11].

For an ideal single-mode cavity, $W_{00} = 1$ and all other $W_{\mu} = 0$. The transverse part of the corresponding Green's function is $\mathcal{D}_{00}(\mathbf{r}, \mathbf{r}') \propto \exp[-(r^2 + r'^2)/w_0^2]$, and the field is $\Phi(\mathbf{r}) \propto \exp(-r^2/w_0^2)$, regardless of $\rho(\mathbf{r}, z)$. Thus, no spatial features of the gas are mapped onto the spatial dependence of the single-mode cavity field.

On the other hand, for a perfect confocal cavity with even parity [49], all $W_{\mu} = 1$ for even $n_{\mu} = l_{\mu} + m_{\mu}$, while $W_{\mu} = 0$ otherwise. This results in the ideal confocal-cavity Green's function [9, 11]:

$$\mathcal{D}(\mathbf{r}, \mathbf{r}', z, z') \propto U^+(\mathbf{r}, \mathbf{r}') \cos(kz) \cos(kz') \quad (4)$$

$$+ U^-(\mathbf{r}, \mathbf{r}') \sin(kz) \sin(kz'), \quad (5)$$

where

$$U^{\pm}(\mathbf{r}, \mathbf{r}') = \delta\left(\frac{\mathbf{r} - \mathbf{r}'}{w_0}\right) + \delta\left(\frac{\mathbf{r} + \mathbf{r}'}{w_0}\right) \pm \frac{1}{\pi} \cos\left[2\frac{\mathbf{r} \cdot \mathbf{r}'}{w_0^2}\right]. \quad (6)$$

The first two terms are the local self-image and mirror image, respectively. The latter arises due to the cavity symmetry [9, 17]. The third is a nonlocal term arising due to Gouy phases: We ignore it for now because it plays only a minor role in cooperativity enhancement (for details, see Appendix A and Refs. [9–11, 38]).

B. Nonideal multimode cavities

1. Finite number of modes

To consider the more physical situation of a *finite* number of modes, we can impose a cutoff at $n_{\mu} = n_c$. This truncates the number of supported cavity modes to approximately account for the finite solid angle subtended by each mirror. While a hard cutoff is conceptually simple, indistinguishable results are obtained using an exponential factor $\exp(-\alpha n_{\mu})$. We employ the latter since it leads to analytical expressions for the Green's function.

Every supermode is a superposition of the modes $\Xi_{\mu}(\mathbf{r})$, weighted by W_{μ} , that have a nonzero amplitude at \mathbf{r} . While no longer a delta function of infinitesimal width, the supermode waist w_{eff} remains smaller than w_0 in proportion to the number of modes in the superposition. Constructive interference increases the local electric field, thereby

enhancing coupling of the atom to light. At the cavity center, the supermode coupling strength g exceeds that of the TEM₀₀ mode by the ratio g/g_0 , which is also the ratio by which the vacuum Rabi splitting between upper and lower polaritons increases when probed on resonance. This leads to a cooperativity enhancement given by Eq. (2).

The number of Ξ_μ that contribute is maximal for the supermode formed at the cavity center and diminishes as \mathbf{r}/w_0 becomes large due to aberrations and finite mirror aperture. Nevertheless, thousands of modes have been observed to contribute in similar confocal cavities [19]. Moreover, w_{eff} can remain smaller than w_0 even at distances many multiples of w_0 away from the cavity center [9]. Modes with high finesse can be observed out to at least $n_\mu = 50$. For simplicity, we assume that κ is constant for all modes but account for the attenuation of finesse through the incorporation of the aforementioned weights W_μ .

2. Imperfect mode degeneracy

High-finesse multimode cavities are also not perfectly degenerate. Inevitable mirror aberrations split mode degeneracy beyond the individual mode line width. This complicates the story, because the atom no longer couples to a cavity eigenmode in the form of a supermode: The collection of modes to which the atom couples are not at the same frequency and therefore do not form an eigenmode. While the use of the term “supermode” remains common in some such contexts (e.g., in near-detuned multimode lasing and superradiance [50,51]) and we have employed it in the past [9,10,20,38], we shift to using the term “synthetic mode.” This modelike entity is defined as the photonic component of the polariton created when the atom coherently couples to all the eigenmodes with field at its position. The field of the synthetic mode is directly accessible through the emission of cavity light. But because it is not an eigenmode, the synthetic mode dephases after a time scale inversely proportional to the frequency spread ω_B when not being pumped.

To analyze this experimentally relevant situation, we consider an atom coupled to near-degenerate modes in the far-detuned configuration $\Delta_C \gg \omega_B$. In an imperfect confocal cavity, the spread of mode frequencies ω_μ within ω_B is more or less random, resulting in an observed bandwidth that depends on the probe beam shape. To avoid the effects of this randomness, one can pump the system far from the near-confocal point and model the modes with a linear dispersion $\omega_\mu = \omega_{00} + \epsilon n_\mu$ [9,11]. For the 1-cm cavities studied below, we measure a mode bandwidth of $\omega_B/2\pi \approx 25$ MHz for the *in situ* cavity and 5 MHz for the *ex situ* cavity [52]. While this is roughly 2 orders of magnitude larger than $\kappa/2\pi = 137$ kHz, enough modes merge within this bandwidth to produce a continuous spectrum [see Fig. 1(b)].

To stimulate a synthetic mode, an electric field satisfying the far-detuning condition may be introduced into the cavity by either longitudinally pumping through a cavity mirror using a spatially mode-matched beam or by transverse pumping via Rayleigh scattering off the atom. Either way, the coherently driven intracavity field manifests as a superposition of near-degenerate modes dispersively coupled to the atom. The cavity emits this synthetic mode at the pump frequency [53]. The notion of a single C_{mm} value is valid only in this dispersive coupling limit, because there is no unique near-resonance vacuum Rabi splitting. Rather, there is a complicated spectrum of mode mixing within the forest of nearly degenerate mode resonances.

We now arrive at the synthetic mode Green’s function, which accounts for both the mode truncation and the mode dispersion within ω_B . The cutoff and linear dispersion are incorporated into the weights $W_\mu = \Delta_C e^{-\alpha n_\mu} / (\Delta_\mu + i\kappa)$; the pump detuning from the near-degenerate modes is Δ_μ . The resulting Green’s function still exhibits a local self-image and mirror image term, both with finite width. The maximum of the synthetic mode Green’s function sets the cooperativity of the cavity, per Eq. (2). The finite width is set by the extent of the synthetic mode, which we now discuss.

C. Spatial imaging and interaction range

The field of the synthetic mode emitted from the cavity may be imaged to provide a spatial map of the photon cloud bound to each atom [9,10]. Cavity emission provides real-time access to the photonic component of the intracavity polariton. Polaritons with overlapping synthetic modes enable the local exchange of photons between nearby atoms. This can mediate interactions among atoms and the waist of the synthetic mode sets this interaction range [9]. This quantity is calculated using the cavity Green’s function $\mathcal{D}(\mathbf{r}, \mathbf{r}')$, as described in Appendix A.

Moreover, if we view the multimode cavity as a lens system, then the minimum spatial width of the synthetic mode is its resolving capability. That is, the point-spread function (PSF) of this “microscope” is proportional to the cavity Green’s function. The local synthetic mode waist directly determines the resolution. We use the half width at half maximum (HWHM) of the field for the resolution metric because its shape does not conform to a standard functional form (see Appendix A). Note that the resolution is always less than the numerical aperture (NA) of the mirrors, because the confocal cavity admits only a quarter of the free-space modes at any given resonance [54].

We now see that the coupling enhancement due to multimode degeneracy increases the cooperativity and improves the imaging resolution as well as introduces an interaction length scale. The narrowness of the synthetic mode waist may be interpreted in two ways. The scale is both an interatom interaction range and the resolving capability

of the mirror system. Moreover, these lengths are naturally matched and so there is no need for higher-resolution imaging. We may consider a multimode cavity to be an unusual “active” quantum gas microscope, in that its fields mediate local interactions among atoms while their emission provides spatial information about atomic positions. We now turn to the experiments that measure the cooperativity enhancement as well as the interaction or resolution length scale.

III. C_{mm} MEASUREMENT SCHEME

Straightforward methods to determine C_{mm} could involve either measuring the synthetic mode light shift or spatially imaging the light emitted from the cavity. Unfortunately, neither method is practicable for our current *in situ* system. The dispersive light shift is too small and direct imaging of the emission suffers from aberrations that obscure the minimum synthetic mode spot size [55]. We revisit the direct-imaging method using an *ex situ* setup designed to circumvent some of these limitations (see Sec. V). Alternative techniques to indirectly image bare-cavity mode shapes (versus supermode or synthetic mode shapes) have been demonstrated using a single ion [56] or arrays of atoms [57].

To measure C_{mm} *in situ*, we use transverse pumping to extract C_{mm} by observing the threshold of superradiant cavity emission. This method was first employed in Ref. [58], where the cooperativity enhancement was interpreted in terms of geometrical optics. Here, we build upon an alternative description from Ref. [9] as well as perform measurements with better spatial resolution than in that work.

To explain this method, we recall that superradiance can emerge via the phase locking of many atomic dipoles when they are transversely pumped above a threshold power. The self-organization threshold is described by the nonequilibrium Hepp-Lieb-Dicke transition (for the Hamiltonian, see Appendix A). Pumping above a critical field strength Ω_c causes the atoms to spontaneously arrange themselves (in position and/or spin [16,59–61]) into one of two possible checkerboard patterns. This forms a phase gradient that Bragg scatters pump photons into the synthetic mode at a rate proportional to the square of the number of intracavity atoms N . Above this threshold, the system condenses into a synthetic mode polariton, the matter component of which is of spin and/or density-wave character. Below threshold, the system incoherently fluctuates between polariton states.

The threshold power scales as $\Omega_c^2 \propto \Delta_C/(NC_{\text{mm}})$, providing a method for measuring C_{mm} . We now employ a more sophisticated theoretical treatment than used in Ref. [9] to extract C_{mm} from Ω_c measurements via the cavity Green’s function. The parameters in the function are determined by analyzing the dependence of the threshold

on different BEC sizes and transverse positions within the cavity. To improve accuracy, we also include higher-order effects and contact interactions.

We now describe how the self-organization threshold for an intracavity BEC depends on Φ and, thus, how C_{mm} can be determined through Eq. (2). As derived in Appendix A, the critical Rabi strength Ω_c of the transverse pump is given by the condition

$$E_{dw} = -\frac{Ng_0^2\Omega_c^2}{\Delta_A^2\Delta_C} \times \Re \left\{ \int d\mathbf{r}\rho(\mathbf{r})\frac{\Phi(\mathbf{r})}{\Phi_0} + \frac{Ng_0^2}{2\Delta_A\Delta_C} \int d\mathbf{r}\rho(\mathbf{r})\frac{\Phi(\mathbf{r})^2}{\Phi_0^2} \right\}, \quad (7)$$

where E_{dw} is the excitation energy of the density wave (set by the atomic recoil and chemical potential) and Δ_A is the atomic detuning of the transverse pump. This field is generated by the scattering of light off the condensate and into the cavity, given by Eq. (1). The pump frequency is always far detuned to the red of the atomic transition frequency ω_A , such that $\Delta_A = \omega_p - \omega_A$ is the largest scale in the Hamiltonian. This renders spontaneous emission negligible on the time scales considered. We also tune the system so that $\Delta_C < 0$.

The first term in parentheses is the atomic density overlap with the intracavity light field and is the standard threshold expression [47]. For better correspondence with experiment, we also consider the second-order term. This describes the overlap with the *intensity* of the cavity light. It represents the leading-order contribution of the dispersive shift. The dispersive shift in a single-mode cavity leads to a simple renormalization of the cavity detuning, $\Delta_C \rightarrow \Delta_C - Ng_0^2 \int d\mathbf{r}\rho(\mathbf{r})\Phi_{00}(\mathbf{r})^2/2\Delta_A\Phi_0^2$. However, it results in a position-dependent correction in a multimode cavity. Furthermore, the dispersive shift contributes even when $\Delta_C/2\pi \approx -100$ MHz because of the localization of light into a synthetic mode.

Thus, by observing the threshold of a BEC with measured shape $\rho(\mathbf{r})$ [62], we can fit the parameters ϵ and α that appear in the Green’s function. This then enables the extraction of \mathcal{D} or, equivalently, Φ , via Eq. (2). Note that we depart from the case of a single intracavity atom when considering superradiant threshold measurements. Since cooperativity is a figure of merit based on the pointlike coupling of light and matter [18], we must assume that the atoms are nearly collocated around \mathbf{r} and ignore (for now) contact interactions among them. (These interactions are incorporated in both the full theory of Appendix A and in the data analysis.) By “nearly,” we mean the experimentally relevant situation of a compact ensemble of N atoms that are maximally and symmetrically coupled to the synthetic mode the waist of which is the smallest supported by the cavity mirrors.

The general setup of the cavity as an active quantum gas microscope is illustrated in Fig. 1(a). A quantum gas with some spatial distribution $\rho(\mathbf{r}, z)$ is placed inside the confocal cavity and illuminated by a transverse pump. We first describe the apparatus and method of quantum gas preparation before discussing the threshold measurements.

A. Cavity apparatus and BEC preparation

The cavity consists of two curved mirrors with radius of curvature $R \approx 1$ cm and $L \approx R$. The single-mode cavity-field emission rate is $\kappa/2\pi = 137$ kHz and, together with a free spectral range of approximately 15 GHz, the cavity has a maximum mode finesse of 55 000. The birefringent splitting of the cavity is observed to be less than κ ; coupling of the scattered pump light to one set of polarization modes is suppressed due to the pump polarization and direction. We realize a single-atom coupling rate of $g_0/2\pi = 1.47$ MHz for ^{87}Rb on the D_2 line [51]. This yields a single-atom single-mode cooperativity of $C = 5.2$.

An ^{87}Rb BEC of approximately 4×10^5 atoms and Thomas-Fermi radii of $[R_x, R_y, R_z] = [11.9(3), 13.2(3), 7.2(1)] \mu\text{m}$ is created inside the cavity using laser cooling and trapping procedures detailed in Refs. [9,10,20,51,60,61]. A more compact BEC shape is necessary to probe the minimum synthetic mode waist. We achieve a smaller-width BEC than used in Ref. [9] by compressing it through the shaping of the crossed optical dipole traps (ODTs) with acousto-optical deflectors (AODs). Specifically, the BEC is compressed to the desired final shape by simultaneously ramping down the dither of the AOD drive frequency while ramping up the ODT power. The BEC probe shapes that we use are either small along the transverse cavity axes, $\{R_x, R_y\} < R_z$, to mimic a pointlike particle [63], or narrow in one direction, $R_x < \{R_y, R_z\}$, for improving the \hat{x} position resolution.

The position \mathbf{r} of the BEC relative to the cavity center is controlled by setting the center frequency of the AOD drive. (The BECs are trapped close to the cavity midplane, $z = 0$.) The final trap shape is characterized by weakly exciting sloshing modes, so that we can measure the trap frequencies through momentum oscillations observed in time-of-flight (TOF) absorption imaging (see the Supplemental Material [64]). The atom number and the BEC position are also measured via TOF imaging. This position calibration is further cross-checked by measuring the superradiance threshold versus \mathbf{r} for a single-mode cavity, where the position dependence is directly related to the known waist of the fundamental mode, w_0 . (We are able to tune the length of the cavity *in situ* to realize a single-mode or confocal configuration [19].)

Once the BEC is positioned, the power of the 780-nm transverse pump beam is linearly ramped over a few milliseconds through the superradiant transition. This beam is set to a detuning of $\Delta_A/2\pi \approx -98$ GHz. We use a

running-wave transverse pump to avoid the formation of a standing-wave lattice, because the standing-wave threshold condition is more complicated than Eq. (7) [65]. This allows us to simplify the relationship between C_{mm} and Ω_c , which is important for reducing systematic error.

The superradiant phase transition is detected by observing the cavity emission on a single-photon counter, heralded by a sudden increase in photon flux at the transition; Fig. 1(c) shows an example. This allows us to extract the critical pump strength Ω_c . The threshold pump power is measured at 35 different positions of the BEC along \hat{x} , ranging from approximately $-17 \mu\text{m}$ to $+17 \mu\text{m}$ and passing through the cavity center. The measurement at each position is repeated typically 4 times. Furthermore, this procedure is repeated for various cavity detunings and with a few different BEC gas shapes to reduce systematic error.

The peak density of the smallest BECs employed reaches $1 \times 10^{15} \text{ cm}^{-3}$. This high density results in significant atom loss during the ramp of the transverse pump. Since the threshold condition depends on the atom number, we calibrate the total atom loss by measuring the atom number at various points throughout the ramp, while suppressing superradiance with increased pump detuning. This allows us to infer the exact atom number at the time of threshold. The observed interaction profile is then fitted using the threshold condition in Eq. (7), given this atom number, the measured trap frequencies (and hence the BEC shape $\rho(\mathbf{r})$ using the Thomas-Fermi approximation), the cavity detuning, and the BEC position. Appendix B describes this fitting procedure in more detail.

IV. MEASUREMENT RESULTS

We now present our measurements of threshold as a function of Δ_C and the BEC probe position.

A. Threshold versus detuning and probe position

Figure 2(a) shows the critical pump strength as a function of Δ_C for three different shapes of a BEC held at the cavity center. We choose to plot the critical pump strength normalized to the typical BEC atom number $N_0 = 3 \times 10^5$. This allows us to plot all three data sets in proximity to each other despite the fact that each is derived from experiments with different BEC populations. The threshold scales with the atom number as $N^{-1/2}$, so the normalized critical pump strength has units of $\sqrt{N_0}$ MHz. The orange data are obtained using the smallest BEC probe we are able to make and provide the most stringent condition for placing an upper bound on the minimum synthetic mode waist supported by the cavity.

The threshold pump strength scales as $\Omega_c \propto \Delta_C^{1/2}$ in a single-mode cavity. This scaling is illustrated in Fig. 2(a) by a black dashed line. However, the scaling is different in a multimode cavity due to the larger number of modes through which the photons may be exchanged. As

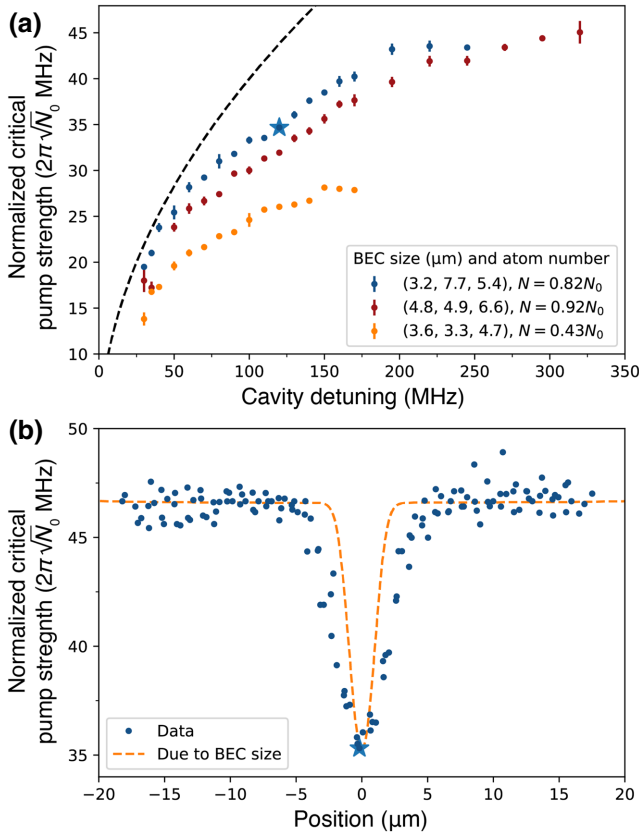


FIG. 2. Threshold measurements. (a) The normalized threshold pump strength $\sqrt{N}\Omega_c$ for a BEC of three different shapes, each located at the cavity center, versus $-\Delta_C/2\pi$. The pump strength is normalized by the typical BEC number, $N_0 = 3 \times 10^5$, and is plotted in units of $2\pi\sqrt{N_0}$ MHz. The BEC radii are listed as (R_x, R_y, R_z) . The required pump power increases with the pump-cavity detuning Δ_C because the photon-mediated interaction becomes weaker. However, the increase is less than in a single-mode cavity due to the participation of high-order modes. The single-mode $\Delta_C^{1/2}$ scaling is shown as a black dashed line. The error bars represent the standard error for five shots per point. (b) The normalized threshold strength as a function of the BEC position. Data are taken at $\Delta_C/2\pi = -120$ MHz, with $N = 0.76N_0$. The dip at the cavity center is due to the interaction enhancement from the overlap of the local and mirror fields [9]. The minimum width of this feature is set by the size of the BEC in \hat{x} ; the BEC probe used here has dimensions $[R_x, R_y, R_z] = [3.1, 7.6, 5.3] \mu\text{m}$, as indicated by the orange dashed line. The fact that the width of the dip exceeds that of the BEC indicates that the synthetic mode has a finite waist. The blue star in each panel corresponds to data taken at the same position, detuning, and trap frequencies.

shown in Fig. 2(a), we do indeed observe a departure from $\Delta_C^{1/2}$ scaling at larger detuning. That is, threshold occurs at lower pump strengths in a confocal cavity. This supports our expectation that a larger interaction energy arises due to the field contribution from these additional modes.

The maximum detuning at which we can take data is limited by both the BEC heating and the atom number. The higher pump power required at large cavity detuning leads to faster BEC heating through incoherent photon scattering. Lower initial atom numbers also require higher pump powers to reach threshold, leading to more heating. Thus, we cannot observe threshold with the least populous BEC beyond 170 MHz (data shown in orange), while we can observe superradiance out to 320 MHz using the most populous BEC (red).

Figure 2(b) plots the threshold pump strength as a function of the BEC position within the cavity. The position of the BEC inside the cavity is scanned in a transverse plane and pumped at a fixed detuning. This is similar to what is done in Ref. [9], though now with a smaller-sized BEC for better resolution. This resolution is sufficiently small that we can now discern the difference between the BEC probe width and the mode waist, as we now discuss.

The threshold strength decreases (the photon-mediated interaction strength increases) at the cavity center due to the overlap of the local and mirror field components [66]. The width of this feature is related to the minimum-detectable spot size of the local field. This measured spot size is larger than the actual minimum synthetic mode waist due to the finite size of the BEC probe. The shape of the BEC is indicated by the dashed line. We can deconvolve the BEC width from the data to obtain a measure of the minimum synthetic mode waist. We use the HWHM of the residual minimum synthetic mode line shape as the resolution of the cavity. We believe that the resolution is limited by the finite extent of the remnant mode-dispersion.

B. Cooperativity enhancement

We next explore by how much the cooperativity is enhanced by the multimode nature of the cavity. As mentioned, this enhancement is captured by the Green's function and, in particular, its on-center value $\mathcal{D}(\mathbf{0}, \mathbf{0})$. Recall that \mathcal{D} is normalized to 1 in a single-mode cavity and hence can be directly interpreted as the enhancement factor C_{mm}/C .

In Fig. 3(a), we show the same data as in Fig. 2(a), except that we scale them by Δ_C to obtain $\mathcal{D}(\mathbf{0}, \mathbf{0})$. The manifest cooperativity enhancement can be qualitatively understood as the result of the modes appearing more degenerate at larger detuning. This allows the modes to form a tighter superposition and a larger electric field at the position of the atoms. All solid curves result from a global theory fit for the parameters ϵ and α . The fit is based on data sets of eight different-shaped BECs (only three are shown here for brevity) as well as 18 scans like the one presented in Fig. 2(b) taken at various detunings and BEC probe shapes. The complete set of data is presented in the Supplemental Material [64].

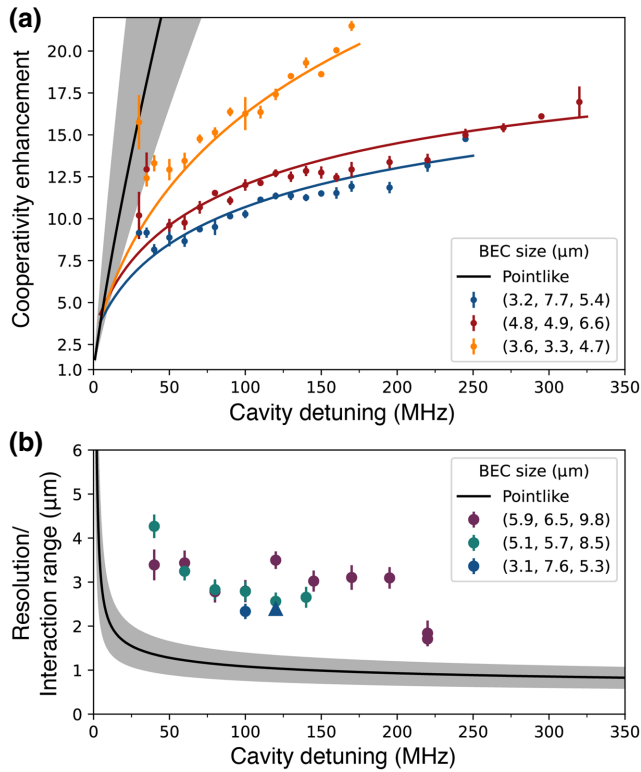


FIG. 3. Cooperativity enhancement and the microscope resolution or interaction range. (a) The data in Fig. 2 presented in terms of multimode cooperativity enhancement. The enhancement increases with detuning and for narrower BECs. All solid lines are derived from the parameters ϵ and α obtained from a single global fit to all measurements via the threshold expression given in Eq. (7). The black curve indicates the enhancement that a point particle would experience at the cavity center. The gray band denotes uncertainty in ϵ and α . The enhancement would reach 96(49) at a detuning of 300 MHz. The maximum directly measured enhancement is 21.5(3). The error bars represent the standard error for five shots per point. (b) The resolution of the multimode cavity, at the cavity center, measured by the HWHM of the synthetic mode profile; see Fig. 2(b) for an example of a profile (convolved with the BEC probe width). This resolution is equivalent to the photon-mediated interaction range [9]. The data points are derived from single scans of the BEC versus position, such as that displayed in Fig. 2(b) (see text for explanation). The microscope reaches a minimum measured resolution of 1.7(2) μm . As in (a), the solid black line and its error band are derived from the global fit to all measurements. The blue triangle corresponds to the data presented in Fig. 2(b).

The fitted theory matches well across all the data sets after applying a global detuning offset Δ_0 and a scale factor to each data set. The offset accounts for uncertainty in identifying the frequency of the lowest-order mode within the transmission spectrum, while the scale factor accounts for systematic uncertainties between data sets in the magnitude of the pump power at threshold. All fit parameters are adjusted to minimize a global reduced χ^2 metric; its minimum is 2.6. The optimal fit parameters

are $\epsilon/2\pi = 2.6$ MHz, $\alpha = 0$, and $\Delta_0/2\pi = 0.8$ MHz and all scale factors are between 1.3 and 2.0. The finite-sized BECs that we use make it difficult to accurately determine the exact value of α . Nevertheless, we can conclude, at a 99% confidence level, that α is smaller than 6×10^{-4} (for further discussion, see Appendix B). This implies that most of the cavity imperfection is due to the imperfect degeneracy of its modes, rather than the finite number of supported modes.

We extrapolate the BEC size down to that of a point particle to estimate cooperativity enhancement limited solely by the cavity. A posterior likelihood distribution for the parameters ϵ and α is used to estimate the probability distribution for the cavity-limited cooperativity at a given cavity detuning. From this, we extract a median and 68% confidence interval [67]. These are shown in Fig. 3(a) as a solid black line and shaded gray region, respectively. At 100-MHz detuning, the estimated cooperativity enhancement for an ideal point particle is 42(22) and it reaches $C_{\text{mm}}/C = 21.5(3)$ at 300-MHz detuning. We conservatively report $C_{\text{mm}}/C = 21.5(3)$ from direct measurements—specifically, the orange data point at 170 MHz—when calculating the maximum multimode cooperativity $C_{\text{mm}} = 112(2)$ that the cavity achieves. To make a rough estimate of the number of modes participating in this cavity, we use a toy model in which a finite number of modes are all perfectly degenerate. By matching the resulting cooperativity to that observed, we estimate that more than one thousand Hermite-Gauss modes participate (for details, see Appendix D).

Before moving on to the resolution measurement, we briefly comment on the nonmonotonicity of the data in Fig. 3(a). There are multiple effects at play at small detunings. All detunings are referenced to an empty cavity. When placing the dispersive medium of atoms inside the cavity, the detunings should be corrected by a dispersive shift that depends on the atom position, atom number, and condensate shape. This effectively reduces the cavity detuning and this shift can be as large as approximately 20 MHz. Operating so close to effective resonance then magnifies other effects. For example, it can be seen in the spectrum shown in Fig. 1(b) that there is not a sharp edge at zero detuning—rather, there is nonzero support for modes at lower frequencies. Interacting resonantly with such modes results in a lower threshold, leading to the observed upturn in the inference of cooperativity enhancement. It is challenging to model these effects successfully, because it requires microscopic understanding of the mode mixing and resonant frequencies, which in turn depend on a detailed knowledge of cavity-mirror imperfections.

C. Microscope resolution and interaction range

We now report the minimum synthetic mode size that the cavity can create. As mentioned above, this length scale

may be interpreted as the photon-mediated interaction range or as the resolution of the cavity microscope.

Position scans such as that in Fig. 2(b) provide a measurement of the cavity-field profile upon deconvolution of the (known) atomic density shape. We show how this provides the length scale of interest in Appendix A 4. The method relies on the assumption that the profile of the cavity field has a Lorentzian shape and that the atomic density kernel is a Gaussian. This allows us to use a Voigt profile for deconvolution. Figure 3(b) shows the resulting resolution or interaction-range estimates at various cavity detunings and various BEC sizes.

To estimate the HWHM of the cavity-limited resolution, we extrapolate to a point particle by using the likelihood distribution of ϵ and α from the global fit, as is done for the cooperativity. The median cavity resolution and 68% confidence interval are shown in Fig. 3(b) as a solid black line and shaded gray region, respectively. Comparing the individual data points derived from the deconvolution method with the solid curve from the global fit, we see that the deconvolution predicts a coarser resolution than that found from the global fit. This might be the result of the aforementioned approximations and/or a biasing effect in the deconvolution process.

At 300 MHz, the extrapolated cavity resolution is $0.9(3) \mu\text{m}$, corresponding to an effective imaging NA of $0.24(7)$. Improvements to mirror quality might improve this but a beyond-paraxial treatment would be necessary to extract resolution when it nears $\lambda = 780 \text{ nm}$. We conservatively report the measured value of $1.7(2) \mu\text{m}$ for the resolution of this cavity, rather than that extrapolated from the global fit.

V. DIRECT IMAGING OF THE SYNTHETIC MODE

We supplement the above with an all-optical scheme for directly observing the cavity properties. While this is not feasible with the present BEC-cavity apparatus, we instead examine an out-of-vacuum cavity of the same configuration. This allows us to observe cavity transmission with a larger geometric NA = 0.42, compared to that of the *in situ* cavity (NA = 0.22). Its cavity mirrors are reflection coated for 741 nm, rather than 780 nm, but they nevertheless possess the same radii of curvature and have a comparable line width of $\kappa/2\pi = 198 \text{ kHz}$ and finesse $\mathcal{F} \approx 38\,000$. This allows us to form a confocal cavity of length $L = 1 \text{ cm}$, just like the *in situ* one. We are able to tune the mirror alignment of this *ex situ* cavity into a more degenerate regime with smaller mode bandwidth ω_B . Whereas the *in situ* cavity possesses a $\omega_B/2\pi \lesssim 25 \text{ MHz}$, we are able to shrink this to approximately 5 MHz in the *ex situ* cavity.

To probe the cavity, a tightly focused longitudinal pump field is injected through the substrate of one cavity mirror. The beam size at the cavity midplane is measured

by removing the second substrate and imaging the waist onto a CCD camera. A minimum waist of $w_p \approx 1.7 \mu\text{m}$ is observed, limited by aberrations from the input cavity substrate and various beam-shaping optics. We characterize these aberrations, allowing us to deconvolve their contributions (see Appendix C 2).

We then replace the second substrate to form the cavity and image the transmitted spot of light. This direct imaging allows us to probe the cavity Green's function: the steady-state cavity field is exactly the convolution of the longitudinal pump with the cavity Green's function (for details, see Appendix C). The action of the Green's function manifests as the broadening of the waist of the cavity transmission after aberrative effects have been removed. This allows us to measure the Green's function through comparison to the single substrate observation.

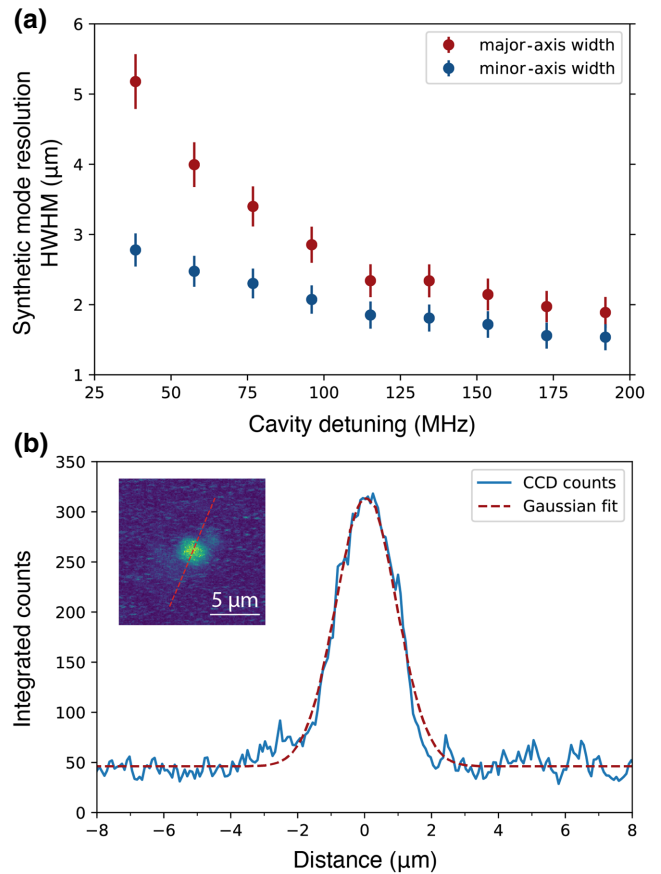


FIG. 4. The all-optical characterization of confocal-cavity resolution. (a) The estimated widths of the cavity Green's function along the major and minor astigmatic axes versus the cavity detuning $-\Delta_C/2\pi$. (b) An example of a typical Gaussian-like intensity profile of the cavity transmission projected onto the minor axis when the probe beam is detuned by approximately 155 MHz. The horizontal axis is the distance in the object plane. The inset shows the full image, with the minor axis indicated by the red dashed line. Together, these clearly demonstrate the ability to image micron-sized features via the cavity.

Specifically, images acquired in transmission are fitted with two-dimensional– (2D) Gaussian profiles and the Gaussian widths of the transmission spot along the principal axes are extracted. Figure 4(b) shows an example of the Gaussian fit along the minor axis for a probe-cavity detuning of 155 MHz. The inset displays the imaged cavity field, with the direction of the minor axis indicated by the red dashed line. From the Gaussian fit, the Green’s function width is then estimated by the convolution relation given in Eq. (C7) of Appendix C. The known pump waist w_p is subtracted to determine the width of the bare-cavity Green’s function, which is finally converted into a HWHM measure of the multimode cavity resolution.

The results versus the cavity detuning are presented in Fig. 4(a). We observe a difference between the widths in the major axis (red points) and minor axis (blue points) of the 2D Gaussian. This difference is likely due to differential strain aberrations caused by the mounts of the mirrors. The width of the Green’s function becomes narrower as detuning increases, in qualitative agreement with the atomic superradiance-threshold measurements. We note that the measured HWHMs only serve as upper bounds. They are limited by the aberrations and finite NA of the postcavity imaging optics, including the output-mirror substrate. The smallest observed width is approximately 2 μm , which is similar to the threshold measurement results. The resolution of this cavity may actually be lower, because we are able to reduce the bandwidth ω_B by a factor of 5 by careful mirror alignment in this *ex situ* test setup. Future work will attempt to place a tighter bound on the minimum cavity resolution and interaction achievable.

VI. CONCLUSIONS

We demonstrate how a transversely pumped confocal cavity can enhance cooperativity through multimode superposition. In addition to inducing strong light-matter coupling, it serves as a microscope for imaging intracavity photon-coupled atoms with a minimum waist of 1.7(2) μm . This is directly matched to the cavity-induced interaction length scale, since they arise from the same cavity field. Thus, as an active quantum gas microscope, this confocal-cavity–QED system yields a high cooperativity of 112(2), while also providing images of intracavity polaritons at their intrinsic interaction length scale.

These results support the notion that pumped confocal cavities can provide a basis for simulating strongly interacting systems such as spin glasses [38], while providing a unique nondestructive channel for observing the microscopic behavior of these systems. An example of such usage has already been demonstrated by imaging a phonon in a dynamical optical lattice realized within this same cavity [20].

ACKNOWLEDGMENTS

We thank Sarang Gopalakrishnan and Yudan Guo for stimulating discussions. We acknowledge funding support from the Army Research Office, NTT Research, and the Next Generation Quantum Science and Engineering (Q-NEXT) U.S. Department of Energy (DOE) National Quantum Information Science Research Center. B.M. acknowledges funding from the Q-NEXT DOE National Quantum Information Science Research Center and the National Science Foundation (NSF) Graduate Research Fellowship.

APPENDIX A: THEORETICAL DESCRIPTION OF THE MULTIMODE SUPERRADIANT TRANSITION FOR A RUNNING-WAVE PUMP

1. Threshold condition

We present a theoretical description of the multimode superradiant transition for the case of the running-wave pump field employed in this work. It closely follows the theory based on standing-wave pumps presented in Ref. [11], with the additional difference that we specialize to the case of a confocal resonator rather than generalize to arbitrary multimode Fabry-Perot cavities.

A system of N atoms with BEC wave function $\Psi(\mathbf{x})$, normalized as $\int d^3\mathbf{x}|\Psi(\mathbf{x})|^2 = 1$, placed inside the cavity is described by the Hamiltonian

$$\begin{aligned} H &= - \sum_{\mu} \Delta_{\mu} \hat{a}_{\mu}^{\dagger} \hat{a}_{\mu} + H_A + H_{LM} \\ H_A &= N \int d^3\mathbf{x} \Psi^*(\mathbf{x}) \left(-\frac{\nabla^2}{2m} + V(\mathbf{x}) + \frac{1}{2} N U_0 |\Psi(\mathbf{x})|^2 \right) \\ &\quad \times \Psi(\mathbf{x}) \\ H_{LM} &= \frac{N}{\Delta_A} \int d^3\mathbf{x} \Psi^*(\mathbf{x}) |\hat{\phi}(\mathbf{x})|^2 \Psi(\mathbf{x}). \end{aligned} \quad (\text{A1})$$

The modes are indexed by μ with pump detuning Δ_{μ} . The photon annihilation operators are \hat{a}_{μ} . $V(\mathbf{x})$ describes the externally applied trapping potential, which is considered to be an anisotropic harmonic trap. The atomic interaction strength $U_0 = 4\pi \hbar^2 a/m$ is proportional to the s -wave scattering length $a = 100a_0$ for ^{87}Rb . The atomic excited state is adiabatically eliminated. H_{LM} is the Stark shift due to the total light field

$$\begin{aligned} \hat{\phi} &= \Omega e^{ik_r x} + \hat{\Phi}(\mathbf{r}), \\ \hat{\Phi}(\mathbf{r}) &= g_0 \sum_{\mu} \hat{a}_{\mu} \Xi_{\mu}(\mathbf{r}) \cos \left[k_r \left(z + \frac{r^2}{2R(z)} \right) - \theta_{\mu}(z) \right]. \end{aligned} \quad (\text{A2})$$

Here, Ω is the Rabi strength of the transverse pump and $k_r = 2\pi/\lambda$ is the recoil momentum in terms of the light

wavelength λ . $\hat{\Phi}$ is the total cavity field and the orthogonal Hermite-Gauss transverse-mode functions are

$$\Xi_{\mu}(\mathbf{r}) = \frac{w_0}{w(z)} H_l \left(\frac{\sqrt{2}x}{w(z)} \right) H_m \left(\frac{\sqrt{2}y}{w(z)} \right) \exp \left[-\frac{r^2}{w(z)^2} \right]. \quad (\text{A3})$$

The single-mode Gaussian beam size is $w(z) = w_0 \sqrt{1 + (\lambda z / \pi w_0^2)^2}$, where w_0 is the waist at the cavity mid-plane. The wave-front curvature is $R(z) = z + \pi^2 w_0^4 / \lambda^2 z$ and $\theta_{\mu}(z)$ is a phase shift defined such that each of the modes satisfies the mirror boundary conditions while also accounting for the Gouy phase. The atoms are centered at longitudinal position z_0 and transverse position \mathbf{r}_0 . Since the atoms are positioned close to the midplane $z = 0$, $z_0 \ll \pi w_0^2 / \lambda$ and we can ignore the wave-front curvature $R(z_0) \rightarrow \infty$. The resulting $\theta_{\mu}(z_0) \approx n_{\mu} \pi / 4$ gives rise to two orthogonal longitudinal quadratures available for atoms to couple. The effect of these quadratures only appears through a nonlocal interaction. To eliminate the effect of the nonlocal interaction that appears in Eq. (6), we choose transverse positions $|\mathbf{r}_0| < w_0 \sqrt{\pi} / 2$. This allows us to focus our analysis on one of the two quadratures. For a more extensive discussion of the physics arising from these longitudinal quadratures, see Ref. [11].

To describe the behavior around the superradiant transition, we must describe only single scattering events. There are two: Scattering a photon from the pump into the cavity or scattering a photon from the cavity back into the pump. To account for these in a running-wave configuration, we make the following ansatz for the atomic wave function:

$$\Psi(\mathbf{x}) = E(\mathbf{x} - \mathbf{x}_0) \left[\psi_0 + \sqrt{2} \cos(k_r z) \times (\psi_F e^{ik_r x} + \psi_B e^{-ik_r x}) \right], \quad (\text{A4})$$

where $E(\mathbf{x} - \mathbf{x}_0)$ is the envelope wave function of the BEC centered at position $\mathbf{x}_0 = (z_0, \mathbf{r}_0)$ and ψ_0 , ψ_F , and ψ_B are amplitudes describing the ground-state fraction and the forward-scattered and the backward-scattered condensate, respectively. In what follows, we suppress the explicit notation of the BEC position (\mathbf{r}_0, z_0) . The normalization condition of the wave function ensures that $|\psi_0|^2 + |\psi_F|^2 + |\psi_B|^2 = 1$.

We evaluate the Hamiltonian in Eq. (A1) using this ansatz. To evaluate the integrals, we assume that the extent of the envelope wave function is large compared to λ , allowing us to drop fast-oscillating terms. We then find the atomic Hamiltonian to be

$$H_A = 2NE_r (|\psi_F|^2 + |\psi_B|^2) + E_{\text{trap}} (|\psi_0|^2 + |\psi_F|^2 + |\psi_B|^2) + E_{\text{int}} \left[|\psi_0|^4 + 4|\psi_0|^2 (|\psi_F|^2 + |\psi_B|^2) + 2\psi_0^2 \psi_F^* \psi_B^* + 2(\psi_0^*)^2 \psi_F \psi_B + \frac{3}{2} (|\psi_F|^4 + |\psi_B|^4 + 4|\psi_F|^2 |\psi_B|^2) \right], \quad (\text{A5})$$

where $E_r = \hbar^2 k^2 / (2m) \approx 3.7$ kHz is the recoil energy, $E_{\text{trap}} = N \int d^3 \mathbf{x} V(\mathbf{x}) E(\mathbf{x})^2$ is the trap energy, and $E_{\text{int}} = \frac{1}{2} N^2 U_0 \int d^3 \mathbf{x} E(\mathbf{x})^4$ is the interaction energy. Using the Thomas-Fermi approximation for the envelope wave function, we can evaluate these integrals [68] to be $E_{\text{trap}} = 3\mu_{\text{TF}} N / 7$ and $E_{\text{int}} = 2\mu_{\text{TF}} N / 7$, where $\mu_{\text{TF}} = (15\hbar^2 a N \omega_x \omega_y \omega_z)^{2/5} m^{1/5} / 2$ is the chemical potential for the Thomas-Fermi cloud expressed in terms of the trap frequencies $\{\omega_x, \omega_y, \omega_z\}$ and atomic properties. For the light-matter interaction, we again drop fast-oscillating terms, which yields [69]

$$H_{\text{LM}} = \frac{N\Omega^2}{\Delta_A} + \frac{Ng_0\Omega}{\sqrt{2}\Delta_A} \left(\sum_{\mu} \hat{a}_{\mu} J_{\mu} \mathcal{O}_{\mu} (\psi_0^* \psi_F + \psi_0 \psi_B^*) + \text{H.c.} \right) + \frac{Ng_0^2}{2\Delta_A} \sum_{\mu, \nu} \hat{a}_{\mu}^{\dagger} \hat{a}_{\nu} J_{\mu, \nu} \mathcal{O}_{\mu} \mathcal{O}_{\nu} + O(\hat{a}^{\dagger} \hat{a} |\psi_{\text{F,B}}|^2), \quad (\text{A6})$$

where $\mathcal{O}_{\mu} = \cos[\theta_{\mu}(z_0)]$, $I_{\mu} = \int dr \rho(\mathbf{r}) \Xi_{\mu}(\mathbf{r})$, and $J_{\mu, \nu} = \int dr \rho(\mathbf{r}) \Xi_{\mu}(\mathbf{r}) \Xi_{\nu}(\mathbf{r})$. $\rho(\mathbf{r}) = \int dz E(\mathbf{x})^2$ is the transverse density distribution. We do not explicitly write out the last term containing two photon operators and two scattered states, as this higher-order term does not affect the threshold condition.

To find the threshold condition, we perform a linear-stability analysis of the normal state $(\psi_0, \psi_F, \psi_B) = (1, 0, 0)$. To do so, we need to ensure that this state is stationary, i.e., that the ψ_0 component has no trivial dynamics associated with it. We do this by subtracting an energy offset to the Hamiltonian of the form $\eta (|\psi_0|^2 + |\psi_F|^2 + |\psi_B|^2)$. This is equivalent to adding a factor $e^{-i\eta t}$ in Eq. (A4), so all atomic components are in a frame rotating at frequency η . We then write the mean-field equations of motion given the total Hamiltonian by taking expectation values $\alpha_{\mu} \equiv \langle \hat{a}_{\mu} \rangle$:

$$\begin{aligned}
i\partial_t \alpha_\mu &= -(\Delta_\mu + i\kappa)\alpha_\mu + \frac{Ng_0\Omega}{\sqrt{2}\Delta_A} I_\mu \mathcal{O}_\mu (\psi_0 \psi_F^* + \psi_0^* \psi_B) + \frac{Ng_0^2}{2\Delta_A} \sum_\nu J_{\mu,\nu} \mathcal{O}_\mu \mathcal{O}_\nu \alpha_\nu, \\
i\partial_t \psi_0 &= (E_{\text{trap}} + E_{\text{int}} (2|\psi_0|^2 + 4|\psi_F|^2 + 4|\psi_B|^2) - \eta) \psi_0 + 4E_{\text{int}} \psi_0^* \psi_F \psi_B + \frac{Ng_0\Omega}{\sqrt{2}\Delta_A} \sum_\mu I_\mu \mathcal{O}_\mu (\alpha_\mu \psi_F + \alpha_\mu^* \psi_B), \\
i\partial_t \psi_F &= (2NE_r + E_{\text{trap}} + E_{\text{int}} (4|\psi_0|^2 + 3|\psi_F|^2 + 6|\psi_B|^2) - \eta) \psi_F + 2E_{\text{int}} \psi_0^2 \psi_B^* + \frac{Ng_0\Omega}{\sqrt{2}\Delta_A} \psi_0 \sum_\mu I_\mu \mathcal{O}_\mu \alpha_\mu^*, \\
i\partial_t \psi_B &= (2NE_r + E_{\text{trap}} + E_{\text{int}} (4|\psi_0|^2 + 6|\psi_F|^2 + 3|\psi_B|^2) - \eta) \psi_B + 2E_{\text{int}} \psi_0^2 \psi_F^* + \frac{Ng_0\Omega}{\sqrt{2}\Delta_A} \psi_0 \sum_\mu I_\mu \mathcal{O}_\mu \alpha_\mu, \quad (\text{A7})
\end{aligned}$$

where we introduce a nonunitary term $-i\kappa\alpha_\mu$ to account for field loss at rate κ . From inspecting the second equation, we see that picking $\eta \equiv E_{\text{trap}} + 2E_{\text{int}} = \mu_{\text{TF}} N$ makes the normal state stationary [68]. Next, since the time scale for the dynamics of the photons is much faster than for the atoms, we can adiabatically eliminate the cavity fields. The last term in the first equation represents the effects of the dispersive shift and while this term can normally be absorbed into Δ_μ , we note that in a multimode cavity it mixes different modes. Because $|Ng_0^2/(2\Delta_A)| \ll |\Delta_\mu|$, we solve the system of coupled modes by treating the coupling perturbatively through the matrix inverse approximation $(1 - A)^{-1} \approx 1 + A$, which is valid when $|\text{eig}(A)| \ll 1$. Then, the instantaneous steady state is

$$\alpha_\mu = \frac{Ng_0\Omega}{\sqrt{2}\Delta_A} (\psi_0 \psi_F^* + \psi_0^* \psi_B) \left[\frac{I_\mu \mathcal{O}_\mu}{\Delta_\mu + i\kappa} + \frac{Ng_0^2}{2\Delta_A} \sum_\nu \frac{J_{\mu,\nu} I_\nu \mathcal{O}_\mu \mathcal{O}_\nu^2}{(\Delta_\mu + i\kappa)(\Delta_\nu + i\kappa)} \right]. \quad (\text{A8})$$

We insert this back into Eq. (A7) along with the choice of η and perform a linear-stability analysis by expanding around the normal state $(\psi_0, \psi_F, \psi_B) = (1, 0, 0) + (\delta\psi_0, \delta\psi_F, \delta\psi_B)$ and keeping only quantities linear in the deviations $\delta\psi$. The equation of motion for $\delta\psi_0$ is trivial, $i\partial_t \delta\psi_0 = 0$, and can be ignored. For the scattered components, we arrive at the coupled system

$$i\partial_t \begin{bmatrix} \delta\psi_F \\ \delta\psi_B \\ \delta\psi_F^* \\ \delta\psi_B^* \end{bmatrix} = \begin{bmatrix} 2NE_r + 2E_{\text{int}} + E_{\text{cav}}^* & 0 & 0 & 2E_{\text{int}} + E_{\text{cav}}^* \\ 0 & 2NE_r + 2E_{\text{int}} + E_{\text{cav}} & 2E_{\text{int}} + E_{\text{cav}} & 0 \\ 0 & -2E_{\text{int}} - E_{\text{cav}} & -2NE_r - 2E_{\text{int}} - E_{\text{cav}} & 0 \\ -2E_{\text{int}} - E_{\text{cav}} & 0 & 0 & -2NE_r - 2E_{\text{int}} - E_{\text{cav}}^* \end{bmatrix} \begin{bmatrix} \delta\psi_F \\ \delta\psi_B \\ \delta\psi_F^* \\ \delta\psi_B^* \end{bmatrix}, \quad (\text{A9})$$

where we introduce the shorthand

$$\begin{aligned}
E_{\text{cav}} &= \frac{N^2 g_0^2 \Omega^2}{2\Delta_A^2} \sum_\mu \frac{I_\mu^2 \mathcal{O}_\mu^2}{\Delta_\mu + i\kappa} + \frac{N^3 g_0^4 \Omega^2}{4\Delta_A^3} \sum_{\mu,\nu} \frac{J_{\mu,\nu} I_\mu I_\nu \mathcal{O}_\mu^2 \mathcal{O}_\nu^2}{(\Delta_\mu + i\kappa)(\Delta_\nu + i\kappa)} \\
&= \frac{N^2 g_0^2 \Omega^2}{2\Delta_A^2 \Delta_C} \left(\int d\mathbf{r} d\mathbf{r}' \rho(\mathbf{r}) \rho(\mathbf{r}') \mathcal{D}(\mathbf{r}, \mathbf{r}') + \frac{Ng_0^2}{2\Delta_A} \int d\mathbf{r} d\mathbf{r}' d\mathbf{r}'' \rho(\mathbf{r}) \rho(\mathbf{r}') \rho(\mathbf{r}'') \mathcal{D}(\mathbf{r}, \mathbf{r}') \mathcal{D}(\mathbf{r}, \mathbf{r}'') \right). \quad (\text{A10})
\end{aligned}$$

The last line follows from inserting the definitions of I_μ and $J_{\mu,\nu}$ and using the definition

$$\mathcal{D}(\mathbf{r}, \mathbf{r}') = \Delta_C \sum_\mu \frac{\Xi_\mu(\mathbf{r}) \Xi_\mu(\mathbf{r}')}{\Delta_\mu + i\kappa} \cos^2[\theta_\mu(z_0)]. \quad (\text{A11})$$

We note that this \mathcal{D} is not quite the same quantity as the three-dimensional (3D) Green's function defined in Eq. (3) but, rather, only the transverse part of it. Indeed, when $z_0 = 0$, $\mathcal{D}(\mathbf{r}, \mathbf{r}') = \mathcal{D}(\mathbf{r}, \mathbf{r}', 0, 0)$.

The system given by Eq. (A9) is unstable when any eigenvalue of the matrix accrues a (positive) imaginary part. Its eigenvalues are given by $\pm\sqrt{4NE_r(NE_r + E_{\text{cav}} + 2E_{\text{int}})}$ and their complex conjugates. Since E_{cav} is complex valued, these eigenvalues have an imaginary part for any (nonzero) pump strength Ω . However, this imaginary part is proportional to $\kappa/(\Delta_C^2 + \kappa^2)$ and since we operate off resonance, where $|\Delta_C| \gg \kappa$, this corresponds to an instability with a growth rate

much slower than the duration of our experiment. Instead, the superradiant threshold is observed when the real part of the argument of the square root becomes negative, resulting in the threshold condition

$$-2\Re\{E_{\text{cav}}\} = 2NE_r + 4E_{\text{int}} = N \left(2E_r + \frac{8}{7}\mu \right) \equiv NE_{d_w}. \quad (\text{A12})$$

This equality is equivalent to the threshold condition presented in the main text as Eq. (7).

Recalling that $\rho(\mathbf{r})$ is centered at the BEC position \mathbf{r}_0 , we note that the threshold is predominantly set by the competition between the photon-mediated self-interaction energy gained at position \mathbf{r}_0 , which is approximately $N^2 g_0^2 \Omega^2 \mathcal{D}(\mathbf{r}_0, \mathbf{r}_0) / \Delta_A^2 \Delta_C$, versus the kinetic and scattering energy cost of self-organization, given by NE_{d_w} . The self-interaction energy is slightly modified due to the finite extent of the cloud; hence the resulting integrals in the threshold condition. The second term in Eq. (7) describes the effect of the multimode dispersive shift due to the BEC at that position.

To find the field inside the cavity that arises after the superradiant transition, we insert Eq. (A8) back into the second line of Eq. (A2). Ignoring the wave-front curvature again, this yields

$$\begin{aligned} \Phi(\mathbf{r}, z) &= \frac{Ng_0^2 \Omega}{\sqrt{2}\Delta_A} (\psi_0 \psi_F^* + \psi_0^* \psi_B) \left(\sum_{\mu} \frac{I_{\mu} \mathcal{O}_{\mu}}{\Delta_{\mu} + i\kappa} \Xi_{\mu}(\mathbf{r}) \cos[k_r z - \theta_{\mu}(z)] \right. \\ &\quad \left. + \frac{Ng_0^2}{2\Delta_A} \sum_{\mu, \nu} \frac{J_{\mu, \nu} I_{\nu} \mathcal{O}_{\mu} \mathcal{O}_{\nu}^2}{(\Delta_{\mu} + i\kappa)(\Delta_{\nu} + i\kappa)} \Xi_{\mu}(\mathbf{r}) \cos[k_r z - \theta_{\mu}(z)] \right) \\ &= \frac{Ng_0^2 \Omega}{\sqrt{2}\Delta_A \Delta_C} (\psi_0 \psi_F^* + \psi_0^* \psi_B) \left(\int d\mathbf{r}' \rho(\mathbf{r}') \mathcal{D}(\mathbf{r}, \mathbf{r}', z, 0) \right. \\ &\quad \left. + \frac{Ng_0^2}{2\Delta_A \Delta_C} \int d\mathbf{r}' d\mathbf{r}'' \rho(\mathbf{r}') \rho(\mathbf{r}'') \mathcal{D}(\mathbf{r}, \mathbf{r}', z, 0) \mathcal{D}(\mathbf{r}', \mathbf{r}'', 0, 0) \right), \end{aligned} \quad (\text{A13})$$

where we again set $z_0 = 0$ to be able to use the 3D Green's functions. In the main text, we define the prefactor as $\Phi_0 \equiv Ng_0^2 \Omega (\psi_0 \psi_F^* + \psi_0^* \psi_B) / (\sqrt{2}\Delta_A \Delta_C)$ and omit the second subleading term.

2. Confocal-cavity Green's function

To derive a more explicit expression for the cavity-induced interaction, we can focus on the midplane of a confocal cavity near an even-mode resonance; that is, where the modes with only even $n_{\mu} = l_{\mu} + m_{\mu}$ participate. At this location, $\mathcal{O}_{\mu} = \cos(n_{\mu}\pi/4)$. As described in the main text, we model the cavity as having a linear dispersion $\Delta_{\mu} = \Delta_C - \epsilon n_{\mu}$ and an exponential mode cutoff $\exp(-\alpha n_{\mu})$. The cavity interaction expression becomes

$$\mathcal{D}(\mathbf{r}, \mathbf{r}') = \Delta_C \sum_{\substack{\mu \\ n_{\mu} \in 2\mathbb{N}_0}} \frac{\Xi_{\mu}(\mathbf{r}) \Xi_{\mu}(\mathbf{r}')}{\Delta_C - \epsilon n_{\mu} + i\kappa} \mathcal{O}_{\mu}^2 e^{-\alpha n_{\mu}} = \sum_{\mu} \frac{\Xi_{\mu}(\mathbf{r}) \Xi_{\mu}(\mathbf{r}')}{1 + \tilde{\epsilon} n_{\mu} + i\tilde{\kappa}} e^{-\alpha n_{\mu}} \cos^2\left(\frac{n_{\mu}\pi}{4}\right) \cos^2\left(\frac{n_{\mu}\pi}{2}\right), \quad (\text{A14})$$

where $\tilde{\epsilon} = -\epsilon/\Delta_C$ and $\tilde{\kappa} = \kappa/\Delta_C$. In the second line, we insert another factor of $\cos^2(n_{\mu}\pi/2)$ to select the appropriate even modes. To convert these sums to integrals, we can use the Green's function for Hermite-Gauss modes:

$$G(\mathbf{r}, \mathbf{r}', t) \equiv \sum_{\mu} \Xi_{\mu}(\mathbf{r}) \Xi_{\mu}(\mathbf{r}') t^{n_{\mu}} = \frac{1}{1-t^2} \exp\left[-\frac{1+t^2}{1-t^2} \frac{\mathbf{r}^2 + \mathbf{r}'^2}{w_0^2} + \frac{4t}{1-t^2} \frac{\mathbf{r} \cdot \mathbf{r}'}{w_0^2}\right]. \quad (\text{A15})$$

The analytical expression on the second line can be found using the Mehler kernel for Hermite polynomials. The interaction strength can then be written as

$$\mathcal{D}(\mathbf{r}, \mathbf{r}') = \int_0^{\infty} d\tau G_{\text{sym}}(\mathbf{r}, \mathbf{r}', e^{-\tilde{\epsilon}\tau - \alpha}) e^{-(1+i\tilde{\kappa})\tau}, \quad (\text{A16})$$

where the mode-selecting cosines are incorporated by symmetrizing the Green's function:

$$4G_{\text{sym}}(\mathbf{r}, \mathbf{r}', t) = G(\mathbf{r}, \mathbf{r}', t) + G(\mathbf{r}, \mathbf{r}', -t) + G(\mathbf{r}, \mathbf{r}', it) + G(\mathbf{r}, \mathbf{r}', -it). \quad (\text{A17})$$

As discussed above, the cavity photon-mediated atom-atom interaction is proportional to $\mathcal{D}(\mathbf{r}, \mathbf{r}')$ [9]. However, the interaction for two identical BECs at positions \mathbf{r}_i and \mathbf{r}_j must account for their finite size. This can be analytically performed by assuming a Gaussian for the density distribution ρ . While the functional form may sometimes be closer to parabolic—i.e., a Thomas-Fermi profile—we numerically verify that using a Gaussian leads to only a very small systematic error in the measurements if the width of the Gaussian is scaled to match the Thomas-Fermi radius. The finite-size-corrected Green's function is then provided by a Gaussian integral. Direct evaluation yields

$$G'(\mathbf{r}_i, \mathbf{r}_j, t) \equiv \int d\mathbf{r} d\mathbf{r}' \rho(\mathbf{r}; \mathbf{r}_i) \rho(\mathbf{r}'; \mathbf{r}_j) G(\mathbf{r}, \mathbf{r}', t) = \frac{(1 + \gamma)^2}{4(1 - \gamma^2 t^2)} \exp\left(-\frac{1 + \gamma}{4(1 - \gamma^2 t^2)} \mathbf{r}_2 \begin{bmatrix} 1 + \gamma t^2 & -(1 + \gamma)t \\ -(1 + \gamma)t & 1 + \gamma t^2 \end{bmatrix} \mathbf{r}_2^T\right), \quad (\text{A18})$$

where $\rho(\mathbf{r}; \mathbf{r}_i) = \exp[-(\mathbf{r} - \mathbf{r}_i)^2 / 2\sigma_A^2] / (2\pi\sigma_A^2)$ is the Gaussian atomic profile centered at \mathbf{r}_i , $\mathbf{r}_2 = \sqrt{2}[\mathbf{r}_i, \mathbf{r}_j] / w_0$, and $\gamma = (1 - 2\sigma_A^2/w_0^2) / (1 + 2\sigma_A^2/w_0^2)$ captures the finite-size effects of an isotropic cloud with Gaussian width σ_A . A generalized result for anisotropic gases, where $\sigma_{A,x} \neq \sigma_{A,y}$, may be similarly derived. The resulting cavity interaction can be found using the analog of Eq. (A16) after symmetrizing G' in the same fashion.

With regard to the last dispersive shift term in Eq. (7), we can use a similar strategy involving the Green's function and Gaussian integrals. The result for an isotropic cloud is

$$\begin{aligned} G^D(\mathbf{r}_i, \mathbf{r}_j, \mathbf{r}_k, t, t') &\equiv \int d\mathbf{r} d\mathbf{r}' d\mathbf{r}'' \rho(\mathbf{r}; \mathbf{r}_i) \rho(\mathbf{r}'; \mathbf{r}_j) \rho(\mathbf{r}''; \mathbf{r}_k) G(\mathbf{r}, \mathbf{r}', t) G(\mathbf{r}, \mathbf{r}'', t') \\ &= \frac{(1 + \gamma)^3}{4a(t, t', \gamma)} \exp\left(-\frac{1 + \gamma}{4a(t, t', \gamma)} \mathbf{r}_3 \begin{bmatrix} 4(1 - \gamma^2 t^2 t'^2) & -2t(1 + \gamma)(1 - \gamma t'^2) & -2t'(1 + \gamma)(1 - \gamma t^2) \\ -2t(1 + \gamma)(1 - \gamma t'^2) & b(t, t', \gamma) & -2(1 - \gamma^2) t t' \\ -2t'(1 + \gamma)(1 - \gamma t^2) & -2(1 - \gamma^2) t t' & b(t', t, \gamma) \end{bmatrix} \mathbf{r}_3^T\right), \end{aligned} \quad (\text{A19})$$

where $\mathbf{r}_3 = \sqrt{2}[\mathbf{r}_i, \mathbf{r}_j, \mathbf{r}_k] / w_0$ and

$$a(t, t', \gamma) = 3 - \gamma(1 + t^2 + t'^2) - \gamma^2(t^2 + t'^2 + t^2 t'^2) + 3\gamma^3 t^2 t'^2, \quad (\text{A20})$$

$$b(t, t', \gamma) = 3 + t^2 - \gamma(1 - t^2)(1 + t'^2) - \gamma^2 t'^2(1 + 3t^2). \quad (\text{A21})$$

Again, this result can be generalized to the case of anisotropic clouds.

Finally, the threshold condition can be explicitly written in terms of the Green's functions:

$$\begin{aligned} E_{dw} &= -\frac{Ng_0^2 \Omega_c^2}{\Delta_A^2 \Delta_C} \Re \left\{ \int_0^\infty d\tau G'_{\text{sym}}(\mathbf{r}_0, \mathbf{r}_0, e^{-\tilde{\epsilon}\tau - \alpha}) e^{-(1+i\tilde{\kappa})\tau} \right. \\ &\quad \left. + \frac{Ng_0^2}{2\Delta_A \Delta_C} \int_0^\infty d\tau \int_0^\infty d\lambda G'_{\text{sym}}(\mathbf{r}_0, \mathbf{r}_0, \mathbf{r}_0, e^{-\tilde{\epsilon}\tau - \alpha}, e^{-\tilde{\epsilon}\lambda - \alpha}) e^{-(1+i\tilde{\kappa})\tau} e^{-(1+i\tilde{\kappa})\lambda} \right\} \\ &= -\frac{Ng_0^2 \Omega_c^2}{\Delta_A^2 \Delta_C} \frac{e^{u\alpha}}{\tilde{\epsilon}} \Re \left\{ \int_0^{e^{-\alpha}} dt G'_{\text{sym}}(\mathbf{r}_0, \mathbf{r}_0, t) t^{u-1} + \frac{Ng_0^2}{2\Delta_A \Delta_C} \frac{e^{u\alpha}}{\tilde{\epsilon}} \int_0^{e^{-\alpha}} dt \int_0^{e^{-\alpha}} dt' G'_{\text{sym}}(\mathbf{r}_0, \mathbf{r}_0, \mathbf{r}_0, t, t') (tt')^{u-1} \right\}, \end{aligned} \quad (\text{A22})$$

where G'_{sym} is symmetrized according to Eq. (A17) with respect to both t and t' arguments and $u \equiv (1 + i\tilde{\kappa}) / \tilde{\epsilon}$. The last line, which follows from a change of the integration variables to t and t' , offers a more convenient expression because it is amenable to numerical evaluation using quadrature techniques [70]. We use a midpoint rule on an inhomogeneous grid to evaluate the threshold for the fits.

3. Cooperativity enhancement

The threshold condition for a single-mode cavity is given by

$$E_{dw} = -\frac{Ng_0^2\Omega_c^2}{\Delta_A^2\Delta_C} \Re \left\{ \int d\mathbf{r}d\mathbf{r}' \rho(\mathbf{r})\rho(\mathbf{r}') \frac{\Xi_{00}(\mathbf{r})\Xi_{00}(\mathbf{r}')}{1+i\tilde{\kappa}} \right\}. \quad (\text{A23})$$

Comparing with the multimode threshold condition in Eq. (7), we note that the (near-)degenerate presence of higher-order modes lowers the threshold by a factor of

$$\frac{C_{\text{mm}}}{C} = \frac{\Re \left\{ \int d\mathbf{r}d\mathbf{r}' \rho(\mathbf{r})\rho(\mathbf{r}') \mathcal{D}(\mathbf{r}, \mathbf{r}') \right\}}{\Re \left\{ \int d\mathbf{r}d\mathbf{r}' \rho(\mathbf{r})\rho(\mathbf{r}') \frac{\Xi_{00}(\mathbf{r})\Xi_{00}(\mathbf{r}')}{1+i\tilde{\kappa}} \right\}}. \quad (\text{A24})$$

To find the cavity-limited enhancement, we first take the limit of a point particle [71] placed at the cavity center, where the light-matter coupling is strongest, $\rho(\mathbf{r}) = \delta(\mathbf{r})$. We then find that $C_{\text{mm}}/C = \Re\{\mathcal{D}(\mathbf{0}, \mathbf{0})\}/\Re\{1/(1+i\tilde{\kappa})\} \approx \mathcal{D}(\mathbf{0}, \mathbf{0})$, because $\tilde{\kappa} \ll 1$. Using the weights $W_\mu = (1 + \tilde{\epsilon}n_\mu + i\tilde{\kappa})^{-1}e^{-\alpha n_\mu}$, this can be expressed as

$$\frac{C_{\text{mm}}}{C} = \frac{1}{4\tilde{\epsilon}} \mathcal{P}\left(e^{-4\alpha}, 1, \frac{u}{4}\right), \quad (\text{A25})$$

where $\mathcal{P}(z, s, a) = \sum_{n=0}^{\infty} z^n (n+a)^{-s}$ is the Lerch transcendent [72].

An extended gas at the cavity center experiences a reduced cooperativity enhancement given by $\int d\mathbf{r}d\mathbf{r}' \rho(\mathbf{r})\rho(\mathbf{r}') \mathcal{D}(\mathbf{r}, \mathbf{r}')$. Using G'_{sym} , we find a similar expression to before,

$$\frac{C_{\text{mm}}^{\text{cloud}}}{C} = \frac{(1+\gamma)^2}{16\tilde{\epsilon}} \mathcal{P}\left(\gamma^4 e^{-4\alpha}, 1, \frac{u}{4}\right). \quad (\text{A26})$$

It is worth noting that other than occurring as the prefactor, γ renormalizes $\alpha \rightarrow \alpha - \ln(\gamma)$. This makes accurate determination of α harder, as finite size obfuscates it. Finally, if the gas is anisotropic, described by $\gamma_{x(y)} = (1 - 2\sigma_{A,x(y)}^2/w_0^2)/(1 + 2\sigma_{A,x(y)}^2/w_0^2)$ for the x (y) direction, we can find the cooperativity enhancement as

$$\frac{C_{\text{mm}}^{\text{aniso}}}{C} = \frac{(1+\gamma_x)(1+\gamma_y)}{8u\tilde{\epsilon}} \left[F_1\left(\frac{u}{2}, \frac{1}{2}, \frac{1}{2}, 1 + \frac{u}{2}, -\gamma_x^2 e^{-2\alpha}, -\gamma_y^2 e^{-2\alpha}\right) + F_1\left(\frac{u}{2}, \frac{1}{2}, \frac{1}{2}, 1 + \frac{u}{2}, \gamma_x^2 e^{-2\alpha}, \gamma_y^2 e^{-2\alpha}\right) \right], \quad (\text{A27})$$

where F_1 is the Appell hypergeometric function [73]. This is the dominant contribution to the theory curves shown in Fig. 3(a), with the remainder coming from the dispersive shift term.

Note that we do not define the multimode cooperativity through a first-principles approach that relates it to the mode volume of $\Phi(\mathbf{r}, z)$. The main reason is that in a multimode cavity with imperfect degeneracy, $\Phi(\mathbf{r}, z)$ represents the field of the *synthetic* mode. It does not exist as an eigenmode at a single optical frequency, due to the dephasing from the dispersion of the constituent bare-cavity modes. That is, this synthetic mode only exists as the photonic part of a coupled light-matter state when the pumping is present, as discussed earlier. Hence, a mode-volume calculation yields an incorrect answer for the enhancement. This subtlety between synthetic mode and supermode disappears when the modes are exactly degenerate.

Indeed, a mode-volume calculation agrees with the above in that case.

4. Atom interaction as a convolution

The position scans as presented in the main text can be approximately understood as a convolution between the local part of the cavity-mediated interaction and a density kernel defined as $\rho_2(\mathbf{r}) = \int d\mathbf{r}' \rho(\mathbf{r}') \rho(\mathbf{r} - \mathbf{r}')$ [9]. Ignoring the nonlocal interaction, we can write $\mathcal{D}(\mathbf{r}, \mathbf{r}') \approx g(\mathbf{r} - \mathbf{r}') + g(\mathbf{r} + \mathbf{r}')$, where $g(\Delta\mathbf{r})$ is the functional form of the local interaction and is (approximately) translationally invariant; the term $g(\mathbf{r} + \mathbf{r}')$ captures the ‘‘mirror’’ image that arises because of the mirror symmetry at an even resonance. Plugging this in and assuming that $\rho(\mathbf{r})$ is symmetric around $\mathbf{r} = \mathbf{r}_0$, we obtain the first integral in the threshold expression given in Eq. (A22):

$$\begin{aligned}
& \int d\mathbf{r}d\mathbf{r}'\rho(\mathbf{r})\rho(\mathbf{r}')\mathcal{D}(\mathbf{r},\mathbf{r}') \\
& \approx \int d\mathbf{z}\rho_2(\mathbf{z})g(\mathbf{z}) + \int d\mathbf{z}\rho_2(\mathbf{z})g(2\mathbf{r}_0 - \mathbf{z}) \\
& = h(\mathbf{0}) + h(2\mathbf{r}_0), \tag{A28}
\end{aligned}$$

where $h(\mathbf{r}) = \int d\mathbf{z}\rho_2(\mathbf{z})g(\mathbf{r} - \mathbf{z})$ is also a convolution.

APPENDIX B: FITTING PROCEDURE

To fit the superradiant threshold data, we rewrite the threshold expression in Eq. (7) as

$$\frac{E_{dw}}{N\Omega_c^2} = -\frac{g_0^2}{\Delta_A^2\Delta_C} \int d\mathbf{r}\rho(\mathbf{r})\Re \left\{ \frac{\Phi(\mathbf{r})}{\Phi_0} + \frac{Ng_0^2}{2\Delta_A\Delta_C} \frac{\Phi(\mathbf{r})^2}{\Phi_0^2} \right\}. \tag{B1}$$

The left-hand side of this equation consists of the observed threshold pump power Ω_c^2 and the atom number at threshold N and forms the dependent variable y . The right-hand side depends on the independent variables $x = \{\mathbf{r}_0, R_x, R_y, \Delta_C\}$, the constants $c = \{g_0, \Delta_A\}$, and the fitting parameters $p = \{\epsilon, \alpha, \Delta_0, \{A_i\}\}$. ϵ and α come in through the weighting factors W_μ of the cavity Green's function as explained in the main text. Δ_0 is an additional offset applied to all cavity detunings because in the nonideal confocal cavity, resonance is not clearly defined. All Δ_C are recorded with respect to a fixed reference point in the cavity transmission spectrum as described in the main text and Δ_0 accounts for mismatch between the arbitrarily chosen reference point and the effective zero-detuning point. The $\{A_i\}$ are overall multiplicative factors for each data set; given the 18 scans and eight on-center data sets, there are a total of 26 such factors. They account for global systematics in the values of Ω and g_0 , as well as systematics between the various data sets in determining the atom number and position. With regard to positioning, each individual scan is corrected for small amounts of residual drift in the BEC position relative to cavity center by fitting the peak with an offset Gaussian and subtracting the offset (Fig. 2(b) is made up of four such individual scans). These corrections are typically 1 μm or less. For these data sets, A still accounts for offsets in the orthogonal direction of similar magnitude.

For the data analysis, we perform a simultaneous least-squares fit to the entire data set to find the optimal fit parameters p^* and their covariance. That is, the fit simultaneously includes all the data taken with various BEC positions and sizes, as well as both of the modalities of measurement presented in Figs. 2(a) and 2(b), respectively. The optimal parameters are $\{\epsilon/2\pi, \alpha, \Delta_0/2\pi\} = \{2.6(1.6) \text{ MHz}, 0(2) \times 10^{-4}, 0.8(18.0) \text{ MHz}\}$, respectively, and the typical amplitude factor is 1.4(4). Note that negative α is unphysical and its reported uncertainty is a one-sided standard deviation.

To cross-check our error estimates, we perform a bootstrap error analysis to ascertain the accuracy of the aforementioned fit. To do so, we draw from the data (with replacement) a random sample of the same total number of data points. The optimal fit parameters are then found again, repeating the process 300 times. We calculate the mean and covariances from the collection of sets of fit parameters. The results are $\epsilon/2\pi = 2.7(1.6) \text{ MHz}$ and $\alpha = 1.4(3.2) \times 10^{-3}$, where the latter is heavily skewed by a small number of outliers (the median α is zero). As we discuss in the main text, our assessment of α is limited by the finite size of the BEC used. In conclusion, the bootstrap estimates of ϵ and the remaining fit parameters are very similar to the fit results reported in the main text.

APPENDIX C: ALL-OPTICAL MEASUREMENT

1. Longitudinal pumping theory

In this appendix, we show that the steady-state cavity response to a longitudinal drive involves the same Green's function that describes the cavity-mediated atom-atom interaction. The Hamiltonian that describes the longitudinal pumping of a multimode cavity is

$$H = -\sum_{\mu} \Delta_{\mu} \hat{a}_{\mu}^{\dagger} \hat{a}_{\mu} + ik(f_{\mu} \hat{a}_{\mu}^{\dagger} - f_{\mu}^* \hat{a}_{\mu}), \tag{C1}$$

where

$$f_{\mu} = \int d\mathbf{r}' \Xi_{\mu}(\mathbf{r}') E_p(\mathbf{r}') \tag{C2}$$

describes the overlap between the longitudinal pump field E_p and the cavity field $\Xi_{\mu}(\mathbf{r})$ at the midplane. Taking into account the cavity photon loss, the expectation values $\alpha_{\mu} = \langle \hat{a}_{\mu} \rangle$ satisfy the following equations of motion:

$$i\partial_t \alpha_{\mu} = -(\Delta_{\mu} + ik)\alpha_{\mu} + ikf_{\mu}. \tag{C3}$$

The steady-state photon fields are derived by setting $\partial_t \alpha_{\mu} = 0$, which yields

$$\alpha_{\mu} = \frac{ikf_{\mu}}{\Delta_{\mu} + ik}. \tag{C4}$$

The transverse-cavity field can be obtained by summing over the amplitudes of the eigenmodes:

$$\begin{aligned}
\Phi(\mathbf{r}) &= \sum_{\mu} \alpha_{\mu} \Phi_{\mu}(\mathbf{r}, z=0) \\
&= ik \int d\mathbf{r}' \sum_{\mu} \frac{\Xi_{\mu}(\mathbf{r}) \Xi_{\mu}(\mathbf{r}')}{\Delta_{\mu} + ik} E_p(\mathbf{r}') \\
&= ik \int d\mathbf{r}' \mathcal{D}(\mathbf{r}, \mathbf{r}') E_p(\mathbf{r}'). \tag{C5}
\end{aligned}$$

This is the same Green's function that describes cavity-mediated interactions between atoms—it has the same

form as Eq. (1). Hence, following the same logic as in Sec. A4, Φ is a convolution of the cavity Green's function \mathcal{D} and the longitudinal pump field E_p .

2. Imaging effects due to cavity substrates

The light field recorded on the camera provides us with the information about the cavity field Φ . However, care must be taken to distill the effect of the Green's function from other imaging aberrations arising from downstream optics. The refraction of the cavity field traveling through a cavity mirror is significant due to its thickness and small radius of curvature. In this work, we are primarily concerned with the on-axis Green's function and so our measurements concentrate on optical spots placed on the mirror substrate near the symmetric axis of the cavity. The major mirror-induced effects are: (1) paraxial lensing that results in demagnification of the field; and (2) aberration effects of the postcavity imaging optics, which modify the PSF to broaden the final image. The field measured at the camera plane can be written as

$$E_{\text{ccd}} = \Theta_{\text{pc}} * (M[\Phi]) = \Theta_{\text{pc}} * (M[\mathcal{D} * E_p]), \quad (\text{C6})$$

where the asterisk (“*”) denotes convolution and $M[x]$ denotes paraxial lensing that transforms $x \rightarrow mx$. $m \approx 0.69$ is the magnification calculated using a paraxial treatment of the cavity substrate. The PSF Θ_{pc} incorporates all the aberration effects from the postcavity imaging optics.

In this analysis, we measure only the intensity of the cavity field, $|E_{\text{ccd}}|^2$, rather than the phase. More could be gleaned by detecting the electric field E_{ccd} using holographic techniques [10,60,74], which we leave for future work. To simplify the analysis of the detected intensity, we approximate Θ_{pc} , \mathcal{D} , and E_p as Gaussians, so that the width of the Green's function can be estimated by taking a quadrature difference:

$$\sigma(\mathcal{D})^2 = \frac{[\sigma(E_{\text{ccd}})^2 - \sigma(\Theta_{\text{pc}})^2]}{m^2} - \sigma(E_p)^2. \quad (\text{C7})$$

For Θ_{pc} , we take into account only on-axis spherical aberrations. This places a lower bound on $\sigma(\Theta_{\text{pc}})$. Hence, the results presented in the main text place a conservative upper bound on $\sigma(\mathcal{D})$ and the cavity resolution.

APPENDIX D: EFFECTIVE MODE NUMBER

We now quantify the effective number of cavity eigenmodes participating in the synthetic mode. To do so, we can use a model with exact degeneracy but a hard cutoff, $l, m \leq M$, where we assume that M is even for convenience. A total of $(M+1)^2/4$ modes can then participate in the synthetic mode. To find the effective value of M , we match the cooperativity enhancement of this model to that

observed. The former can be calculated by explicitly summing the Hermite-Gauss modes at the cavity center while accounting for the mode selection via

$$W_{l,m} = \begin{cases} 1, & \text{if } l+m = 0 \pmod{4}, \\ 0, & \text{otherwise.} \end{cases} \quad (\text{D1})$$

In accordance with Eq. (2) this gives

$$\begin{aligned} \frac{C_{\text{square}}}{C} &= \sum_{l=0}^M \sum_{m=0}^M \Xi_{l,m}(\mathbf{0})^2 W_{l,m} \\ &= 2^{-2M-1} \frac{(M+1)!^2}{(M/2)!^4} \\ &\quad + 2^{-M-1} \frac{(M+1)!^2}{(M/2)!^2} {}_2F_1\left(-\frac{M}{2}, \frac{1}{2}, \frac{3}{2}, 2\right)^2 \\ &\approx \frac{1}{\pi} M + \frac{2}{\pi} + \sqrt{2} + \mathcal{O}(M^{-1}), \end{aligned} \quad (\text{D2})$$

where ${}_2F_1$ is a hypergeometric function [73], and the approximation holds for large M . Thus, to match the highest observed cooperativity enhancement ratio of $C_{\text{mm}}/C \approx 21$, we need $M \approx \pi C_{\text{mm}}/C \approx 66$ and the number of participating modes is $1/4(M+1)^2 \approx 1100$. We note that while this effective number of modes depends on the exact form of the cutoff used, the order of magnitude and scaling with C_{mm} are generic.

-
- [1] S. Haroche, J. Raimond, and O. U. Press, *Exploring the Quantum: Atoms, Cavities, and Photons, Oxford Graduate Texts* (Oxford University Press, Oxford, 2006).
 - [2] T. E. Northup and R. Blatt, Quantum information transfer using photons, *Nat. Photon* **8**, 356 (2014).
 - [3] A. Reiserer and G. Rempe, Cavity-based quantum networks with single atoms and optical photons, *Rev. Mod. Phys.* **87**, 1379 (2015).
 - [4] J. Borregaard, E. J. Davis, G. S. Bentsen, M. H. Schleier-Smith, and A. S. Sørensen, One- and two-axis squeezing of atomic ensembles in optical cavities, *New J. Phys.* **19**, 093021 (2017).
 - [5] A. Blais, A. L. Grimsmo, S. Girvin, and A. Wallraff, Circuit quantum electrodynamics, *Rev. Mod. Phys.* **93**, 025005 (2021).
 - [6] S. Gopalakrishnan, B. L. Lev, and P. M. Goldbart, Emergent crystallinity and frustration with Bose-Einstein condensates in multimode cavities, *Nat. Phys.* **5**, 845 (2009).
 - [7] S. Gopalakrishnan, B. L. Lev, and P. M. Goldbart, Frustration and Glassiness in Spin Models with Cavity-Mediated Interactions, *Phys. Rev. Lett.* **107**, 277201 (2011).
 - [8] A. González-Tudela, C.-L. Hung, D. E. Chang, J. I. Cirac, and H. J. Kimble, Subwavelength vacuum lattices and atom-atom interactions in two-dimensional photonic crystals, *Nat. Photon.* **9**, 320 (2015).

- [9] V. D. Vaidya, Y. Guo, R. M. Kroeze, K. E. Ballantine, A. J. Kollár, J. Keeling, and B. L. Lev, Tunable-Range, Photon-Mediated Atomic Interactions in Multimode Cavity QED, *Phys. Rev. X* **8**, 011002 (2018).
- [10] Y. Guo, R. M. Kroeze, V. D. Vaidya, J. Keeling, and B. L. Lev, Sign-Changing Photon-Mediated Atom Interactions in Multimode Cavity Quantum Electrodynamics, *Phys. Rev. Lett.* **122**, 193601 (2019).
- [11] Y. Guo, V. D. Vaidya, R. M. Kroeze, R. A. Lunney, B. L. Lev, and J. Keeling, Emergent and broken symmetries of atomic self-organization arising from Gouy phase shifts in multimode cavity QED, *Phys. Rev. A* **99**, 053818 (2019).
- [12] J. A. Muniz, D. Barberena, R. J. Lewis-Swan, D. J. Young, J. R. K. Cline, A. M. Rey, and J. K. Thompson, Exploring dynamical phase transitions with cold atoms in an optical cavity, *Nature* **580**, 602 (2020).
- [13] A. Periwal, E. S. Cooper, P. Kunkel, J. F. Wienand, E. J. Davis, and M. Schleier-Smith, Programmable interactions and emergent geometry in an array of atom clouds, *Nature* **600**, 630 (2021).
- [14] Z. Li, B. Braverman, S. Colombo, C. Shu, A. Kawasaki, A. F. Adiyatullin, E. Pedrozo-Peñafiel, E. Mendez, and V. Vuletić, Collective Spin-Light and Light-Mediated Spin-Spin Interactions in an Optical Cavity, *PRX Quantum* **3**, 020308 (2022).
- [15] X. Zhang, E. Kim, D. K. Mark, S. Choi, and O. Painter, A superconducting quantum simulator based on a photonic-bandgap metamaterial, *Science* **379**, 278 (2023).
- [16] F. Mivehvar, F. Piazza, T. Donner, and H. Ritsch, Cavity QED with quantum gases: New paradigms in many-body physics, *Adv. Phys.* **70**, 1 (2021).
- [17] A. E. Siegman, *Lasers* (University Science Books, Sausalito, California, 1986).
- [18] H. J. Kimble, Strong interactions of single atoms and photons in cavity QED, *Phys. Scr.* **T76**, 127 (1998).
- [19] A. J. Kollár, A. T. Papageorge, K. Baumann, M. A. Armen, and B. L. Lev, An adjustable-length cavity and Bose-Einstein condensate apparatus for multimode cavity QED, *New J. Phys.* **17**, 043012 (2015).
- [20] Y. Guo, R. M. Kroeze, B. P. Marsh, S. Gopalakrishnan, J. Keeling, and B. L. Lev, An optical lattice with sound, *Nature* **599**, 211 (2021).
- [21] L. W. Clark, N. Schine, C. Baum, N. Jia, and J. Simon, Observation of Laughlin states made of light, *Nature* **582**, 41 (2020).
- [22] C. Baum, M. Jaffe, L. Palm, A. Kumar, and J. Simon, Optical mode conversion via spatiotemporally modulated atomic susceptibility, *Opt. Express* **31**, 528 (2022).
- [23] S. Gopalakrishnan, B. L. Lev, and P. M. Goldbart, Atom-light crystallization of Bose-Einstein condensates in multimode cavities: Nonequilibrium classical and quantum phase transitions, emergent lattices, supersolidity, and frustration, *Phys. Rev. A* **82**, 043612 (2010).
- [24] V. Torggler and H. Ritsch, Adaptive multifrequency light collection by self-ordered mobile scatterers in optical resonators, *Optica* **1**, 336 (2014).
- [25] V. Torggler, I. Krešić, T. Ban, and H. Ritsch, Self-ordering and cavity cooling using a train of ultrashort pulses, *New J. Phys.* **22**, 063003 (2020).
- [26] F. Mivehvar, S. Ostermann, F. Piazza, and H. Ritsch, Driven-Dissipative Supersolid in a Ring Cavity, *Phys. Rev. Lett.* **120**, 123601 (2018).
- [27] S. Schuster, P. Wolf, S. Ostermann, S. Slama, and C. Zimmermann, Supersolid Properties of a Bose-Einstein Condensate in a Ring Resonator, *Phys. Rev. Lett.* **124**, 143602 (2020).
- [28] J. Léonard, A. Morales, P. Zupancic, T. Esslinger, and T. Donner, Supersolid formation in a quantum gas breaking a continuous translational symmetry, *Nature* **543**, 87 (2017).
- [29] J. Léonard, A. Morales, P. Zupancic, T. Donner, and T. Esslinger, Monitoring and manipulating Higgs and Goldstone modes in a supersolid quantum gas, *Science* **358**, 1415 (2017).
- [30] C. Rylands, Y. Guo, B. L. Lev, J. Keeling, and V. Galitski, Photon-Mediated Peierls Transition of a 1D Gas in a Multimode Optical Cavity, *Phys. Rev. Lett.* **125**, 010404 (2020).
- [31] K. E. Ballantine, B. L. Lev, and J. Keeling, Meissner-Like Effect for a Synthetic Gauge Field in Multimode Cavity QED, *Phys. Rev. Lett.* **118**, 045302 (2017).
- [32] P. Strack and S. Sachdev, Dicke Quantum Spin Glass of Atoms and Photons, *Phys. Rev. Lett.* **107**, 277202 (2011).
- [33] M. Buchhold, P. Strack, S. Sachdev, and S. Diehl, Dicke-model quantum spin and photon glass in optical cavities: Nonequilibrium theory and experimental signatures, *Phys. Rev. A* **87**, 063622 (2013).
- [34] V. Erba, M. Pastore, and P. Rotondo, Self-Induced Glassy Phase in Multimodal Cavity Quantum Electrodynamics, *Phys. Rev. Lett.* **126**, 183601 (2021).
- [35] S. Gopalakrishnan, B. L. Lev, and P. M. Goldbart, Exploring models of associative memory via cavity quantum electrodynamics, *Philos. Mag.* **92**, 353 (2012).
- [36] P. Rotondo, M. Marcuzzi, J. P. Garrahan, I. Lesanovsky, and M. Müller, Open quantum generalisation of Hopfield neural networks, *J. Phys. A: Math. Theor.* **51**, 115301 (2018).
- [37] E. Fiorelli, M. Marcuzzi, P. Rotondo, F. Carollo, and I. Lesanovsky, Signatures of Associative Memory Behavior in a Multimode Dicke Model, *Phys. Rev. Lett.* **125**, 070604 (2020).
- [38] B. P. Marsh, Y. Guo, R. M. Kroeze, S. Gopalakrishnan, S. Ganguli, J. Keeling, and B. L. Lev, Enhancing Associative Memory Recall and Storage Capacity Using Confocal Cavity QED, *Phys. Rev. X* **11**, 021048 (2021).
- [39] H. Tanji-Suzuki, I. D. Leroux, M. H. Schleier-Smith, M. Cetina, A. T. Grier, J. Simon, and V. Vuletić, Interaction between atomic ensembles and optical resonators, *Adv. At., Mol., Opt. Phys.* **60**, 201 (2011).
- [40] g_0 is measured with respect to the peak field of the Gaussian TEM₀₀ mode at the cavity center.
- [41] J. M. Raimond, M. Brune, and S. Haroche, Manipulating quantum entanglement with atoms and photons in a cavity, *Rev. Mod. Phys.* **73**, 565 (2001).
- [42] K. M. Birnbaum, A. Boca, R. Miller, A. D. Boozer, T. E. Northup, and H. J. Kimble, Photon blockade in an optical cavity with one trapped atom, *Nature* **436**, 87 (2005).
- [43] N. Jia, N. Schine, A. Georgakopoulos, A. Ryou, L. W. Clark, A. Sommer, and J. Simon, A strongly interacting polaritonic quantum dot, *Nat. Phys.* **14**, 550 (2018).

- [44] Y.-T. Chen, M. Szurek, B. Hu, J. de Hond, B. Braverman, and V. Vuletić, High finesse bow-tie cavity for strong atom-photon coupling in Rydberg arrays, *Opt. Express* **30**, 37426 (2022).
- [45] While we employ the term “mode waist,” we actually mean the HWHM of the field. This is because the synthetic modes are not simple Hermite-Gaussians and so lack the same definition of mode waist as discussed in, e.g., Ref. [17].
- [46] D. Chang, J. Douglas, A. González-Tudela, C.-L. Hung, and H. Kimble, Colloquium: Quantum matter built from nanoscopic lattices of atoms and photons, *Rev. Mod. Phys.* **90**, 031002 (2018).
- [47] P. Kirton, M. M. Roses, J. Keeling, and E. G. Dalla Torre, Introduction to the Dicke model: From equilibrium to nonequilibrium, and vice versa, *Adv. Quantum Technol.* **2**, 1800043 (2018).
- [48] The full mode function may also possess a nonlocal component that is discussed below [9–11].
- [49] Confocal resonators support purely even- or odd-parity mode families every other half free-spectral-range [17]. We consider only even-mode families throughout this work.
- [50] E. Kapon, J. Katz, and A. Yariv, Supermode analysis of phase-locked arrays of semiconductor lasers, *Opt. Lett.* **9**, 125 (1984).
- [51] A. J. Kollár, A. T. Papageorge, V. D. Vaidya, Y. Guo, J. Keeling, and B. L. Lev, Supermode-density-wave-polariton condensation with a Bose-Einstein condensate in a multimode cavity, *Nat. Commun.* **8**, 14386 (2017).
- [52] To measure the bandwidth, we use a 7- μm -waist probe beam in the cavity center and define ω_B as the full width at 30% maximum of the transmission.
- [53] Light shifts modify this frequency but are insignificant compared to κ for the far-detuned system considered below.
- [54] Only transversely even or odd modes and only longitudinally sine or cosine modes are supported at each degenerate resonance [10,11,17].
- [55] One could determine the minimum synthetic mode waist by longitudinally driving the cavity with ever smaller beam waists. However, in our present experimental system, imaging the cavity emission does not reveal the limit of cavity performance due to aberrations from the cavity substrate and low downstream-imaging NA.
- [56] G. R. Guthöhrlein, M. Keller, K. Hayasaka, W. Lange, and H. Walther, A single ion as a nanoscopic probe of an optical field, *Nature* **414**, 49 (2001).
- [57] E. Deist, J. A. Gerber, Y.-H. Lu, J. Zeiher, and D. M. Stamper-Kurn, Superresolution Microscopy of Optical Fields Using Tweezer-Trapped Single Atoms, *Phys. Rev. Lett.* **128**, 083201 (2022).
- [58] A. T. Black, H. W. Chan, and V. Vuletić, Observation of Collective Friction Forces due to Spatial Self-Organization of Atoms: From Rayleigh to Bragg Scattering, *Phys. Rev. Lett.* **91**, 203001 (2003).
- [59] K. Baumann, C. Guerlin, F. Brennecke, and T. Esslinger, Dicke quantum phase transition with a superfluid gas in an optical cavity, *Nature* **464**, 1301 (2010).
- [60] R. M. Kroeze, Y. Guo, V. D. Vaidya, J. Keeling, and B. L. Lev, Spinor Self-Ordering of a Quantum Gas in a Cavity, *Phys. Rev. Lett.* **121**, 163601 (2018).
- [61] R. M. Kroeze, Y. Guo, and B. L. Lev, Dynamical Spin-Orbit Coupling of a Quantum Gas, *Phys. Rev. Lett.* **123**, 160404 (2019).
- [62] This is determined by trap-frequency measurements and corroborated by atomic absorption imaging.
- [63] The extent along \hat{z} is irrelevant to the cooperativity, as enhancement is only due to confinement of the synthetic mode in the transverse direction.
- [64] See the Supplemental Material at <http://link.aps.org/supplemental/10.1103/PRXQuantum.4.020326> for information on BEC characterization and the full data set.
- [65] This is because the band structure of the standing-wave optical potential causes the density-wave energy E_{dw} to be dependent on pump power. Consequently, the threshold condition would have to be solved self-consistently.
- [66] The reduction in threshold pump strength depends on atom number and cavity detuning due to the position-dependent dispersive shift term but is nominally $1/\sqrt{2}$ due to the doubled field strength when the local and mirror fields overlap.
- [67] The distributions are not Gaussian and feature long tails. Hence, we report the median and confidence interval rather than mean and standard deviation.
- [68] C. Pethick and H. Smith, *Bose-Einstein Condensation in Dilute Gases* (Cambridge University Press, Cambridge, 2002).
- [69] On the second line, we should write $\cos(\theta_\mu - \theta_\nu) = \mathcal{O}_\mu \mathcal{O}_\nu + \sin(\theta_\mu) \sin(\theta_\nu)$ but we can omit the sin terms as they all evaluate to zero for the mode indices of interest.
- [70] P. J. Davis and P. Rabinowitz, *Methods of Numerical Integration* (Orlando, Academic Press, 1984).
- [71] $N = 1$ for a point particle; hence we omit the dispersive shift term from Eq. (7) in the above expression for C_{mm} because its contribution is negligible.
- [72] T. M. Apostol, in *NIST Handbook of Mathematical Functions*, edited by F. W. J. Olver, D. W. Lozier, R. F. Boisvert, and C. W. Clark (Cambridge University Press, 2010) p. 612.
- [73] R. A. Askey and A. B. Olde Daalhuis, in *NIST Handbook of Mathematical Functions*, edited by F. W. J. Olver, D. W. Lozier, R. F. Boisvert, and C. W. Clark (Cambridge University Press, 2010), p. 384.
- [74] N. Schine, M. Chalupnik, T. Can, A. Gromov, and J. Simon, Electromagnetic and gravitational responses of photonic Landau levels, *Nature* **565**, 173 (2019).

Correction: An error in the inline equation appearing in the second sentence of the last paragraph of Sec. II B was introduced during the production cycle and has been fixed.